The Geological Society Special Publications

Miocene UHT granulites from Seram, eastern Indonesia: a geochronological-REE study of zircon, monazite, and garnet

--Manuscript Draft--

Manuscript Number:	GSLSpecPub17-257R3
Article Type:	Chapter
Full Title:	Miocene UHT granulites from Seram, eastern Indonesia: a geochronological-REE study of zircon, monazite, and garnet
Short Title:	Miocene UHT granulites from Seram
Corresponding Author:	Jonathan Mark Pownall Australian National University Canberra, ACT AUSTRALIA
Corresponding Author E-Mail:	jonathan.pownall@anu.edu.au
Other Authors:	Richard A Armstrong
	Ian S Williams
	Matthew F Thirlwall
	Christina J Manning
	Robert Hall
Order of Authors (with Contributor Roles):	Jonathan Mark Pownall (Conceptualization: Lead; Data curation: Equal; Formal analysis: Lead; Funding acquisition: Lead; Investigation: Lead; Methodology: Supporting; Project administration: Lead; Validation: Equal; Visualization: Lead; Writing – original draft: Lead; Writing – review & editing: Lead)
	Richard A Armstrong (Data curation: Lead; Formal analysis: Lead; Investigation: Equal; Methodology: Equal; Resources: Equal; Writing – review & editing: Equal)
	Ian S Williams (Data curation: Equal; Formal analysis: Lead; Investigation: Equal; Methodology: Lead; Resources: Equal; Software: Equal; Validation: Equal; Writing – review & editing: Equal)
	Matthew F Thirlwall (Data curation: Equal; Formal analysis: Equal; Investigation: Equal; Methodology: Lead; Resources: Lead; Supervision: Equal; Writing – review & editing: Supporting)
	Christina J Manning (Data curation: Equal; Formal analysis: Lead; Investigation: Equal; Methodology: Equal; Resources: Equal; Supervision: Equal; Validation: Equal; Writing – review & editing: Equal)
	Robert Hall (Conceptualization: Equal; Funding acquisition: Lead; Investigation: Supporting; Methodology: Supporting; Project administration: Equal; Resources: Equal; Supervision: Lead; Validation: Supporting; Writing – original draft: Supporting; Writing – review & editing: Supporting)
Abstract:	The island of Seram, eastern Indonesia, incorporates Miocene ultrahigh-temperature (UHT; > 900˚C) garnet-sillimanite granulites that formed by extensional exhumation of hot mantle rocks behind the rolling-back Banda Arc. UHT metamorphic conditions are supported by new Zr-in-rutile thermometry results, and the Miocene age of the UHT event is confirmed by closely-matched HREE abundances between garnet and c. 16 Ma zircon. Monazites also record identical U-Pb ages, within uncertainty. However, these geochronometers do not date peak UHT metamorphism; instead, they date retrograde, garnet-consuming (Zr- and REE-liberating) reactions that produced the granulites' post-peak cordierite + spinel reaction microstructures. Zircons shielded within garnet did not crystallize c. 16 Ma rims, and so were unaffected by the entire UHT event. Miocene UHT metamorphism overprinted a Late Triassic-Early Jurassic upper-amphibolite facies event that grew garnet cores and 216-173 Ma zircon. In the Miocene, these garnet cores were overgrown by peritectic garnet rims during UHT metamorphism, with some rutiles recording ~900˚C Zr-in-rutile temperatures. Garnet

	Lu-Hf ages of 138 Ma—produced by core-rim mixing—demonstrate that a component of Hf4+ produced since c. 200 Ma was retained through the c. 16 Ma UHT event. Accordingly, UHT conditions must have been very short-lived and exhumation of the granulite complex very rapid.
Section/Category:	Metamorphic Geology: Microscale to Mountain Belts
Additional Information:	
Question	**Response**
Are there any conflicting interests, financial or otherwise?	No
Samples used for data or illustrations in this article have been collected in a responsible manner	Confirmed

for: Ferrero, S., Lanari, P., Gonclaves, P., Grosch, E.G. (Eds.), Metamorphic Geology – Microscale to Mountain Belts. Geological Society, London, Special Publications

Miocene UHT granulites from Seram, Indonesia: a geochronological–REE study of zircon, monazite, and garnet

J.M. Pownall[1,2]*, R.A. Armstrong[1], I.S. Williams[1], M.F. Thirlwall[3], C.J. Manning[3], & R. Hall[2]

RESPONSE TO REVIEWERS:

Dear Pierre,

As requested, we've addressed all minor comments that you suggested.

best wishes,
Jon

for: Ferrero, S., Lanari, P., Gonclaves, P., Grosch, E.G. (Eds.), Metamorphic Geology – Microscale to Mountain Belts. Geological Society, London, Special Publications

Miocene UHT granulites from Seram, eastern Indonesia: a geochronological–REE study of zircon, monazite, and garnet

J.M. Pownall[1,2]*, R.A. Armstrong[1], I.S. Williams[1], M.F. Thirlwall[3], C.J. Manning[3], & R. Hall[2]

[1]*Research School of Earth Sciences, Australian National University, Canberra, ACT 2601, Australia*
[2]*SE Asia Research Group, Department of Earth Sciences, Royal Holloway University of London, Egham TW20 0EX, UK*
[3]*Department of Earth Sciences, Royal Holloway University of London, Egham TW20 0EX, UK*

**Corresponding author (e-mail: jonathan.pownall@anu.edu.au)*

J.M.P., 0000-0002-6013-3193
R.A.A., 0000-0002-3062-0679
I.S.W., 0000-0003-4465-6493
R.H., 0000-0003-1693-6914

short title: Miocene UHT granulites from Seram

word count: 9051

Abstract: The island of Seram, eastern Indonesia, incorporates Miocene ultrahigh-temperature (UHT; > 900˚C) garnet–sillimanite granulites that formed by extensional exhumation of hot mantle rocks behind the rolling-back Banda Arc. UHT metamorphic conditions are supported by new Zr-in-rutile thermometry results, and the Miocene age of the UHT event is confirmed by closely-matched HREE abundances between garnet and *c*. 16 Ma zircon. Monazites also record identical U–Pb ages, within uncertainty. However, these geochronometers do not date peak UHT metamorphism; instead, they date retrograde, garnet-consuming (Zr- and REE-liberating) reactions that produced the granulites' post-peak cordierite + spinel reaction microstructures. Zircons shielded within garnet did not crystallize *c*. 16 Ma rims, and so were unaffected by the entire UHT event. Miocene UHT metamorphism overprinted a Late Triassic–Early Jurassic upper-amphibolite facies event that grew garnet cores and 216–173 Ma zircon. In the Miocene, these garnet cores were overgrown by peritectic garnet rims during UHT metamorphism, with some rutiles recording ~900˚C Zr-in-rutile temperatures. Garnet Lu–Hf ages of 138 Ma—produced by core–rim mixing—demonstrate that a component of Hf^{4+} produced since c. 200 Ma was retained through the c. 16 Ma UHT event. Accordingly, UHT conditions must have been very short-lived and exhumation of the granulite complex very rapid.

Supplementary material: Zircon REE data (SHRIMP), and garnet REE data (LA-ICP-MS) are available at >>>.

Ultrahigh-temperature (UHT; >900˚C) granulites were produced in eastern Indonesia by extension following the Miocene collision of Australia with SE Asia (Pownall *et al.* 2014). These rocks, exposed on the island of Seram (Fig. 1, 2), record the youngest of only ~60 known instances when the geothermal gradient was elevated locally beyond the UHT threshold of 700˚C GPa^{-1} (Brown 2006, 2014; Harley 2008, 2016; Kelsey 2008; Kelsey & Hand 2015). Importantly, the Seram UHT

granulites occur within the same tectonic system that generated the UHT conditions, thereby enabling detailed study of their formation mechanism without complications introduced by multiple overprinting deformational and metamorphic episodes. This is in contrast to the vast majority of UHT terranes that reside in Proterozoic cratons and whose tectonic drivers remain far more elusive (Kelsey & Hand 2015). As such, these young Indonesian granulites offer a unique opportunity to investigate (*i*) how UHT conditions may be generated by the modern Earth; and (*ii*) potential *P–T* paths and metamorphic rates experienced by high-grade metamorphic rocks in modern arc settings.

The Seram UHT granulites comprise part of the Kobipoto migmatite complex (Pownall 2015; Pownall *et al.* 2017*a*) – a suite of garnet- and cordierite-bearing diatexites hosting garnet–sillimanite–cordierite–spinel residua (following migmatite terminology of Sawyer 2008). The residual assemblage features spinel + quartz inclusions within garnet, and quartz-absent sapphirine + corundum + spinel symplectite within cordierite (Fig. 3). Phase equilibria modelling of the Al–Fe-rich granulite melanosome (Pownall 2015) indicated peak *P–T* conditions of 925˚C and 9 kbar for the interpreted peak model assemblage garnet + sillimanite + spinel + ilmenite + plagioclase + silicate melt. A clockwise *P–T* path through these peak conditions (Fig. 4) was interpreted to descend steeply down-pressure from garnet-present to cordierite-present fields to account for the most dominant discontinuous retrograde reaction interpreted to have affected the assemblage: garnet + sillimanite → cordierite + spinel ± quartz, at 7–6 kbar (Fig. 4), which developed the granulites' characteristic ordered reaction microstructures (Fig. 3). But when, and how rapidly, did metamorphism occur? And what was the tectonic driver for the metamorphism and subsequent exhumation?

Two critical observations from field mapping (Pownall *et al.* 2013, 2016) explain how UHT conditions on Seram were attained. First of all, the granulites and associated diatexites always coexist with voluminous lherzolites (Pownall *et al.* 2017*a*). And secondly, this granulite–lherzolite complex has been exhumed by considerable extension beneath low-angle detachment faults, still at high enough temperatures to have generated partial melting in the hanging wall (Pownall *et al.* 2017*b*). Initially interpreted to comprise part of an ophiolite (e.g., Linthout *et al.* 1996), these lherzolites have an exhumed subcontinental lithospheric mantle origin, and their rapid juxtaposition against shallower crustal rocks (at 35 km depth, to correspond with peak metamorphic pressure) was sufficient to have elevated crustal temperatures into the UHT regime (Fig. 4; Pownall *et al.* 2017*a*).

The island of Seram is located in the northern limb of the Banda Arc (Fig. 1), beneath which an inwardly concave slab of Jurassic oceanic lithosphere has been subducted (Spakman & Hall 2010; Hall 2011, 2017, 2018; Pownall *et al.* 2016). The extremely curved geometry of the Banda Arc and its underlying slab was achieved by subduction rollback, whereupon collapse of the down-going slab drove southeastward migration of the subduction hinge-line and adjacent trench. As depicted by regional plate reconstructions (e.g., Hall 2012), Banda slab rollback drove oceanic spreading within the trailing Banda Sea as well as continental rifting and hot hyperextension within the fringes of the Australian continental margin (the 'Sula Spur', of which Seram is derived). A compilation of $^{40}Ar/^{39}Ar$ ages dating shear-zone movements on Seram (Pownall *et al.* 2017*b*) and oceanic spreading histories of the Banda Sea basins (Hinschberger *et al.* 2000, 2001) demonstrate that Banda Arc rollback commenced around 16 Ma before propagating southeastwards towards Australia. The latest phase of this rollback-driven extension from 2 Ma 'rolled open' the 7 km Weber Deep basin in the easternmost Banda Sea, further exhuming lherzolites across a chain of small islands bordering the abyss (Pownall *et al.* 2016).

Zircon U–Pb dating of the Seram UHT granulite residuum and associated diatexites (Pownall *et al.* 2014, 2017*a*) revealed 3 separate age populations (Fig. 5; Table 1): (*i*) ages obtained for detrital cores between 3.4 Ga and 216 Ma; (*ii*) a broad spread of ages obtained from core-truncating overgrowths between 215 and 173 Ma; and (*iii*) a population of *c*. 16 Ma ages obtained from a 2nd zircon overgrowth (although some ages from this third group are as old as 25 Ma). Furthermore, $^{40}Ar/^{39}Ar$ ages obtained for biotite are within uncertainty of the respective zircon U–Pb ages for the

same samples, implying exceptionally rapid cooling rates (Pownall et al., 2017*b*). The close correlation between these latest *c*. 16 Ma zircon U–Pb ages with the inferred timing of Banda rollback initiation at *c*. 16 Ma, in light of the tectonic interpretation borne from field observations that UHT conditions were achieved by extreme lithospheric extension, led us to conclude previously that UHT metamorphism occurred at 16 Ma synchronous with the initial phase of extension behind the rapidly rolling-back Banda slab (Pownall et al., 2014, 2017*a*; Pownall 2015). But how robust is this inference for the timing of the UHT event? For instance, how certain are we that UHT metamorphism did not instead occur within the 216–170 Ma window recorded by the oldest zircon overgrowth event? Could we further test our hypotheses using additional geochronometers? And, if so, could we integrate the results of different dating techniques with trace element systematics operating during the rocks' metamorphism and melting? These questions provided the motivation behind this current study.

Here, we present new monazite U–Pb, garnet Lu–Hf, and garnet Sm–Nd data, accompanied by rare-earth element (REE) analyses of zircon and garnet plus new Ti-in-zircon and Zr-in-rutile thermometry results. These new data indeed substantiate previous findings that UHT metamorphism on Seram occurred at *c*. 16 Ma, and provide further quantification of the granulite complex's rapid metamorphism and exhumation history.

Tectonic and metamorphic context

Lower-crustal–upper-mantle rocks that comprise the Kobipoto Complex (Pownall 2015) are exposed across Seram (specifically western Seram, the Kobipoto Mountains of central Seram, and the Wai Leklekan Mountains of eastern Seram), and within the chain of small islands of Kasiui, Tioor, Kur, and Fadol curving round to the easternmost part of the arc (Valk 1945; Germeraad 1946; van der Sluis 1950; Hamilton 1979; Bowin *et al.* 1980; Charlton *et al.* 1991; Honthaas *et al.* 1997; Pownall *et al.* 2016). No ultramafic rocks or UHT granulites were found by the authors on Buru (Fig. 1), although it is possible that they are present in the shallow sub-surface (Linthout *et al.* 1989).

Most of the metamorphic rocks on Seram (Fig. 2) are chlorite- to kyanite-grade metapelites and intercalated mafic amphibolites belonging to the Tehoru Formation (Tjokrosapoetro & Budhitrisna 1982), which correlates with the Wahlua Complex on Buru (Linthout *et al.* 1989). The Tehoru Formation was deposited in the Late Triassic to Early Jurassic (Pownall *et al.* 2017*a*), metamorphosed at up to upper amphibolite facies at *c*. 17 Ma, and then subjected to localized deformational events until 3.3 Ma by the operation of major strike-slip fault systems accommodating Banda slab rollback (Pownall *et al.* 2017*b*).

Migmatites featuring garnet-sillimanite granulites, and lherzolites intruded by the migmatites, together comprise the Kobipoto Complex (Pownall 2015; Pownall *et al.* 2017*a*). In western Seram (the Kaibobo and Hoamoal peninsulas; Fig. 2), Kobipoto Complex rocks occur beneath low-angle detachment faults, immediately above which are 500 m-thick high-temperature shear zones characterized by sillimanite-defined shear banding and localized partial melting (Pownall *et al.* 2013, 2017*b*). We interpret these high-*T* mylonites (which comprise the Taunusa Complex) to have formed in response to high-temperature exhumation of hot Kobipoto Complex lherzolites and migmatites beneath the detachment (Pownall *et al.* 2013, 2017*a*, *b*). As outlined by Pownall *et al.* (2013, 2014, 2017*a*), we therefore consider that the lherzolites must have been exhumed from the subcontinental mantle, and so were never part of an ophiolite.

In the Kobipoto Mountains, central Seram (Fig. 2)—the sampling location of granulites investigated in this paper—migmatites and lherzolites have been exhumed within a left-lateral positive flower structure (Pownall & Hall 2014). This structure is a part of the larger 120–300˚-trending Kawa Fault Zone that bisects Seram (Pownall *et al.* 2013), which itself is a member of the larger Seram–Kumawa Shear Zone (Hall *et al.* 2017). This shear zone system accommodated the

differences in motion between the southeastward-rolling Banda trench (Spakman & Hall 2010) and the adjacent Sula Spur promontory of the Australian continental margin.

The Kobipoto Complex granulites

The Kobipoto Complex is exposed in western Seram, in the Wai Leklekan Mountains of eastern Seram, and on Ambon (Fig. 2). Kobipoto Complex migmatites comprise leucosome-rich diatexites peppered with small schlieren of sillimanite + spinel and contain abundant cordierite and garnet phenocrysts (Priem *et al.* 1978; Pownall 2015; Pownall *et al.* 2017*a*). These diatexites, along with lherzolites with which they share direct contacts, were exhumed beneath detachment faults in western Seram at 5.8–5.6 Ma, and on Ambon at 3.5–3.3 Ma (Pownall *et al.* 2017*a*, *b*).

In the Kobipoto Mountains of central Seram, the migmatites contain a higher proportion of residual granulite, and stromatic metatexites are therefore more common. Scarce occurrences of highly residual garnet-sillimanite granulite (Fig. 3), described in detail by Pownall (2015), are also present. As mentioned previously, these granulites contain garnet-hosted composite inclusions of spinel + quartz (± ilmenite ± sillimanite) (Fig. 3c), and post-peak quartz-absent symplectites of sapphirine + corundum + spinel within cordierite that formed during a near-isothermal decompression stage of a clockwise *P–T* path (Fig. 4; Pownall *et al.* 2014; Pownall 2015). A THERMOCALC *P–T* pseudosection (Powell & Holland 1988) for the residual assemblage indicated peak metamorphic conditions of 925 ± 50˚C at 9 ± 1 kbar (Pownall 2015). Through the post-peak discontinuous reaction garnet + sillimanite → cordierite + spinel ± quartz (Hensen & Green 1971), the Seram granulites developed prominent reaction microstructures featuring coronae of cordierite containing spinel + corundum ± sapphirine ± sillimanite symplectites (Fig. 3a, b, e, f), which formed at 754 ± 116˚C and 4 ± 1 kbar (Pownall 2015).

Sample Petrography

The samples analysed as part of this study—KP11-588 and KP11-619—were both collected from the Wai Tuh river gorge in the Kobipoto Mountains at [129.479˚E, 3.002˚S] and [129.474˚E, 3.017˚S], respectively (Fig. 2):

- ***Garnet–sillimanite granulite KP11-588*** (Fig. 3a–c) is a highly residual granulite, containing abundant garnet (~25 vol.%) and prismatic sillimanite (~20 vol.%) separated by ordered reaction microstructures comprising cordierite coronae and cordierite + spinel ± ilmenite ± corundum ± sapphirine symplectites (Fig. 3a, b, e). Plagioclase and quartz also feature within some cordierite coronae as narrow, vermicular intergrowths (Fig. 3e). Ilmenite is fairly abundant (5–10 vol.%) and occurs as inclusions within garnet and also as coarse grains bordering spinel (Fig. 3b). Coexisting spinel + quartz (± corundum) occurs as small inclusions within garnet (Fig. 3c). These composite inclusions are interpreted to have formed by localised reactions consuming former sillimanite and ilmenite inclusions with garnet (Pownall 2015).
- ***Garnet–cordierite–sillimanite metatexite KP11-619*** (Fig. 3d, f) features abundant melanosome comprising cordierite + biotite + garnet + sillimanite. Garnets are large (sometimes > 5 mm) and cordierite is typically pinitized. Some of the fresher cordierite contains sprays of sillimanite needles and biotite. Compared to sample KP11-588, this rock contains a far higher proportion of leucosome (~ 60 vol.%).

Textural locations of zircon, monazite, and rutile

Zircon and monazite both occur throughout the rock (*i*) as inclusions within garnet; (*ii*) within post-peak reactions microstructures in which garnet has been replaced by cordierite + spinel; (*iii*) within sillimanite; and (*iv*) within the leucosome (Fig. 6a–d). Both zircon and monazite grains are larger and more abundant within the cordierite coronae and leucosome than as inclusions within garnet. Rutile occurs both as inclusions within garnet and within the leucosome, adjacent to garnet (Fig. 6e, f).

Melt inclusions within garnet

We report melt inclusions (MIs) within some garnets of sample KP11-588, identified by optical microscopy (Fig. 7). The MIs, which are < 10 μm diameter, are characterized by their square cross-sections, composite interiors, and distinctive rims (Fig. 7b). The mineralogy of individual domains are unfortunately too small to determine optically, although the overall appearance of the MIs do seem to resemble polycrystalline nanogranitoids (Cesare *et al.* 2015). The MIs are clustered in large groups that are distributed sporadically throughout some garnets (Fig. 7a). Many garnets do not host MIs, and only a small minority host MIs larger than 5 μm. In addition to these primary MIs, smaller and blebbier MIs occur along planar fractures through the garnet (red arrow in Fig. 7a), which we interpret as secondary features.

We interpret the widespread occurrence of primary MIs as further evidence that (most) garnet must have grown in the presence of melt as a solid peritectic product of melt-producing reactions. This conclusion is consistent with the result from phase equilibria modelling (Pownall 2015) that both peak metamorphism and high-temperature retrogression occurred above the solidus (Fig. 4). As shown in Fig. 6a, zircon is present in garnets that also host MIs, suggesting that some zircons and other accessory minerals may have been entrapped in garnet in the presence of melt.

SHRIMP U–Pb zircon geochronology

Zircon U–Pb ages for Kobipoto Complex granulites and diatexites were measured previously by Pownall *et al.* (2014, 2017*a*) using sensitive high-resolution ion microprobes SHRIMP-II and SHRIMP-RG (reverse geometry) at the Research School of Earth Sciences (RSES), Australian National University (ANU), Canberra. See Pownall *et al.* (2017*a*) for detailed analytical and data reduction methods. Cathodoluminescence (CL) images (Fig. 8) were acquired for all zircons mounted in epoxy for U–Pb dating at the RSES using a CL hyperspectral imaging system paired with a Cameca SX-100 electron microprobe. In order to provide petrographic context, CL images were also acquired at the RSES for zircons *in situ* within a thin section of sample KP11-588 (Fig. 9) using a CL detector paired with a JEOL 6610A SEM (15 kV, 1μm-diameter beam).

Zircons from the Kobipoto Complex show complex internal structures arising from multiple growth and dissolution events. These relationships are illustrated by the CL images and cartoon zircons presented in Figure 8. Typically, a zircon from the residual granulites (e.g., sample KP11-588) will feature a detrital core around which are two distinct overgrowths, identified from CL images due to different CL responses and their cross-cutting relationships. Following Pownall *et al.* (2017*a*), we have used the following scheme to describe different parts of the zircon grains:

- C_d — detrital zircon cores;
- C_m — magmatic or metamorphic cores (sample dependant);
- R_m — magmatic or metamorphic zircon rims (sample dependant);
- R_2 — an inner CL-bright rim between outer R_m rims and C_d cores (or sometimes as the only rim around C_d cores);
- R_o — very thin CL-bright overgrowths (that were too small to analyse).

The U–Pb zircon geochronology results of Pownall *et al.* (2017*a*) are detailed in Table 1 and Figure 5. In summary, detrital cores (C_d) are aged between 3.4 Ga and 216 Ma; R_2 overgrowths yielded ages between 215 and 173 Ma; and younger R_m rims are *c.* 16 Ma.

An important new finding, revealed by the *in situ* CL imaging, is that zircons included within garnet *do not* have *c*. 16 Ma R_m rims (Fig. 9b–e). These younger rims are present only on zircons located in the post-peak reaction microstructures and the leucosome (Fig. 9a). Zircons in all textural settings feature *c*. 200 Ma R_2 zones around detrital C_d cores. These relationships are consistent across a total of 26 zircon grains imaged *in situ* using CL.

SHRIMP U–Pb monazite geochronology

To complement previous zircon U–Pb dating, monazite was analysed *in situ* from a gold-coated polished thin section of sample KP11-588 using SHRIMP-II at the RSES, ANU. Analyses were performed using a 10 kV primary beam of O_2^- ions focused on the sample surface over a 30 μm spot diameter. Monazite standard '44069' (424.9 ± 0.4 Ma; Aleinikoff *et al.* 2006) was used for calibration. The data were reduced using the SQUID-2 Excel macro (Ludwig 2009) utilising decay constants from Steiger & Jäger (1977), and concordia diagrams were plotted using Isoplot-3 (Ludwig 2003). The correction for common Pb was made using ^{207}Pb (which assumes $^{206}Pb/^{238}U$–$^{207}Pb/^{235}U$ concordance) and the relevant initial $^{207}Pb/^{206}Pb$ value from the model of Stacey & Kramers (1975).

Monazite was analysed from two textural settings: (*i*) from a large monazite grain within the leucosome (grain 1; Fig. 6c); and (*ii*) from a monazite inclusion within garnet (grain 2; Fig. 6d). All four analyses yielded within uncertainty the same $^{206}Pb/^{238}U$ age (Table 2), and define an isochron date of 16.4 ± 0.4 Ma (Fig. 10). This date is within analytical uncertainty of the mean $^{206}Pb/^{238}U$ age of R_m zircon from the same sample (16.0 ± 0.6 Ma).

Garnet and zircon geochemistry

Garnet major element chemistry

Garnet major element chemistry was measured previously using a JEOL JXA-8100 Superprobe electron microprobe (EPMA) paired with an Oxford Instruments INCA EDS system at Birkbeck College, University of London (Pownall 2015). Mineral EPMA analyses used an accelerating voltage of 15 kV, a beam current of 10 nA, a 1 μm beam diameter, and were calibrated using natural silicate and oxide standards before a ZAF correction procedure was applied.

As shown in Figure 11, broad and compositionally homogeneous garnet core regions are dominantly an almandine–pyrope solid solution (X_{alm}~ 0.60; X_{pyr}~ 0.30; X_{sps}~ 0.06; X_{grs}~ 0.04). Moderate zoning is present in the outermost margin, with almandine increasing (X_{alm} rising from 0.60 to 0.68) and pyrope decreasing (X_{pyr} falling from 0.30 to 0.17) moving towards the rim. The replacement of original garnet rims by cordierite coronae during high-*T* retrogression (Fig. 3e) is further evidenced by the truncation of garnet zoning profiles, as shown by the backscatter intensity map in Figure 11b. A sharp increase of Mn (spessartine) close to the rim demonstrates that garnet resorption occurred during cordierite corona development.

Garnet REE analysis

REE zonation profiles for several garnets in sample KP11-588 were measured *in situ* from a polished thin section by rim-to-core-to-rim laser traverses using the RESOlution M-50 193 mm ArF excimer laser (40 μm spot size) coupled to an Aglient 7500ce LA-ICP-MS system (Müller *et al.* 2009) at

Royal Holloway University of London (RHUL). NIST SRM-612 glass was used as an external standard. The variation in Lu, Hf, Sm, and Nd for one of these traverses is shown in Figure 12, and the full range of REE abundances is plotted in Figure 13. The full dataset is included in the supplement.

These REE profiles demonstrate the occurrence of chemically-distinct core regions (shaded grey in Fig. 12), which interestingly are *not* shown by the major element distributions. Core REE concentrations are substantially higher (> 10×) than those of the rims (e.g., ~1 ppm ^{175}Lu in the rim; ~30 ppm ^{175}Lu in the core). In the example shown in Figure 12, the diameter of the garnet core is ~45% of the entire crystal, and so volumetrically the core regions represent only ~9 vol% of the garnet as a whole (or even smaller if considering that the outermost garnet rims have since been consumed to produce the cordierite + spinel coronae).

Zircon REEs and Ti

SHRIMP II at Geoscience Australia, Canberra, was used to analyse R_m and R_2 zircon from samples KP11-588 and KP11-619 for Ti and Rare Earth Element (REE) abundances. These analyses used the same zircon mount that was used previously for U–Pb geochronology, and so zircon grains and analytical spots correlate with those reported by Pownall *et al.* (2017*a*).

For these analyses, a 10 kV primary O_2^- ion beam was used to ablate spots *c.* 25 μm diameter. Positive secondary ions were extracted at 10 kV and mass analysed at approximately R5000. Moderate energy filtering of the secondary ions (*c.* 20% transmission of ^{91}Zr) was used to reduce the contribution of potential isobaric interferences, particularly from LREE oxides. All REE were measured, and for those REE that were not monoisotopic, two isotopes were measured as a check on accuracy. Other isotopes analysed were ^{49}Ti (for the Ti-in-zircon thermometry), ^{46}SiO (to ensure accurate location of the ^{49}Ti peak), ^{91}Zr (as a reference for calculating the REE concentrations), and two Hf isotopes (for the calculation of Zr/Hf). Relative sensitivity factors for Ti, the REE and Hf were calculated from an initial analysis of NIST611 glass, and SL13 and Temora 2 zircons were analysed as secondary standards. Each analysis consisted of three scans through the isotopes of interest, which took 15 minutes. The data were reduced using an in-house Excel spreadsheet. Analytical uncertainties ranged from *c.* ± 2 ppb for REE isotopes with low concentrations (< 20 ppb) to *c.* ± 0.2 ppm for REE isotopes with high concentrations (> 50 ppm).

Eight sets of analyses were acquired from the two samples: one R_m zircon rim and three R_2 zircon zones for sample KP11-588; and four R_m zircon rims for sample KP11-619 (see supplementary data). As shown in Figure 13, R_m and R_2 zircon have very distinct REE profiles: (*i*) R_2 zircon has over an order of magnitude greater enrichment in the heavy REEs (HREEs) than R_m zircon (e.g., maxima of 78 ppm Lu for R_2, and 3 ppm for R_m); and (*ii*) R_m zircon has notably flatter light REE (LREE) profiles than R_2.

Zircon Th/U ratios

For the Kobipoto Mountains granulite samples, R_m zircon rims all have Th/U ratios < 0.1 (Fig. 14). Assuming that the Th/U values in this instance can be considered a reliable discriminator of magmatic versus metamorphic zircon, where Th/U < 0.1 suggests a metamorphic origin (Rubatto 2002), then the R_m rims for the granulites exclusively plot in the 'metamorphic zone'. The detrital cores have higher Th/U ratios than the rims, some of them surpassing 1. The R_2 zircon zones display a wide spread in Th/U ratios that mostly plot in the 'metamorphic' field (Th/U < 0.1) but some analyses show similar values to the detrital cores (Th/U approaching 1).

Since different populations of zircon are consistently grouped based on their Th/U ratios, and zircons with known magmatic origin have the highest values, we consider it likely that the *c.* 16 Ma R_m zircon rims with notably lower Th/U ratios crystallized during a metamorphic episode, in

accordance with previous conclusions (Pownall *et al.* 2014, 2017*a*). To a lesser extent, this trend is also indicative of the R_2 zircon being also metamorphic in origin.

Zircon–rutile thermometry

Following Ferry & Watson (2007), the exchanges of Ti^{4+} between zircon and rutile (and/or other Ti-bearing phases), and of Zr^{4+} between rutile and zircon (and/or other Zr-bearing phases) may be utilized as geothermometers. As zircon and rutile grains occur in the same microtextural domains—both as inclusions within garnet and in the leucosomes of the Kobipoto Complex granulites (Fig. 6, 9)—it is reasonable to assume in this instance that rutile and zircon were in (or close to) equilibrium.

Ti-in-zircon thermometry

Using the Ti abundances acquired to high precision by SHRIMP (methodology detailed in previous section), the Ti-in-zircon thermometry calibrations of Watson *et al.* (2006) and Ferry & Watson (2007) were applied to granulite samples KP11-588 and KP11-619 (Fig. 15; Table 3). Based on the Ferry & Watson (2006) thermometer, R_m zircons crystallized at temperatures of *c.* 600˚C (540–640˚C); and R_2 zircon at slightly higher temperatures of *c.* 700˚C (660–750˚C). The Watson *et al.* (2006) thermometer gave similar temperatures, but with much larger positive uncertainties (of +200˚C).

Despite these samples having attained peak metamorphic temperatures of *c.* 925˚C, neither R_m nor R_2 zircon shows evidence for having crystallized under or even close to UHT conditions. One possible reason for these lower-than-expected temperatures is if $a\mathrm{TiO_2}$, assumed here to be 1.0, was overestimated (Yakymchuk *et al.* 2017). Although there is evidence in this instance for rutile and zircon co-inhabiting the same domains of the rock, it is still possible that a lower $a\mathrm{TiO_2}$ was in operation. For a metapelite of broadly similar composition to the Seram UHT granulites, and for similar *P–T* conditions to the formation of their post-peak reaction microstructures (900˚C and 7 kbar, with melt present), Yakymchuk *et al.* (2017) calculated an $a\mathrm{TiO_2}$ value of ~0.7. However, using this lower $a\mathrm{TiO_2}$ value raised our Ferry & Watson (2006) Ti-in-zircon temperatures by only ~30ºC – a long way short of raising these estimates to peak UHT conditions.

These results imply that R_m metamorphic zircon must have crystallized during retrogression after the peak of UHT metamorphism (so at 600˚C and *c.* 3 kbar, based on the *P–T* path inferred by Pownall 2015), and not under peak metamorphic conditions (even if a much lower $a\mathrm{TiO_2}$ value were used). Temperatures of *c.* 700˚C for the R_2 zircon are consistent with either a high-grade metamorphic or a magmatic origin during crystallisation at *c.* 200 Ma (with low Th/U ratios indicative of the former; Fig. 14).

Zr-in-rutile thermometry

Rutile was analysed *in situ* from a polished thin section (most grains < 30 μm) using a 193 nm Coherent excimer laser (focused to a 13 μm beam diameter) coupled to a Aglient 7700 ICP-MS at the RSES, ANU. NIST-610 glass was used as the primary standard, and NIST-612 and BCR-2G glasses were used as secondary standards. Data were reduced using Iolite software (Paton *et al.* 2011) following the "semi-quantitative" data reduction scheme.

Twenty analyses were acquired (after discarding misplaced spots) for rutiles occurring as inclusions within garnet, and adjacent to garnet from within the cordierite-dominated coronae. Zr-in-rutile temperatures were calculated using the Ferry & Watson (2007) and Tomkins *et al.* (2007) thermometers for an $a\mathrm{SiO_2}$ of 1 and a pressure of 9 kbar. Both calibrations yielded identical results within uncertainty (Table 4).

Figure 16 shows the results of the Tomkins *et al.* (2007) thermometer. The most Zr-rich rutile grain (3816 ± 365 ppm Zr; Fig. 6f) corresponds to a Zr-in-rutile temperature of 907 ± 14˚C. A total of three analyses indicated temperatures in the vicinity of 900˚C, although most temperature fall between 600 and 750˚C (Fig. 16). Interestingly, those highest temperatures were recorded by rutile grains within the leucosome, with rutile included in garnet (e.g. Fig. 6e) recording the significantly lower temperatures. These hottest rutile grains indicate temperatures consistent with having recorded peak metamorphic conditions of 925˚C and 9 kbar (Pownall 2015).

Lu–Hf and Sm–Nd garnet geochronology

Garnet preparation for isotope dilution

Garnets were separated from the melanosome of sample KP11-588 at RHUL from a 63–250 μm diameter crushed rock fraction (the same fraction from which the zircon was separated) using sodium polytungstate heavy-liquid floatation, Frantz magnetic separation, and hand picking beneath a binocular microscope. Care was taken to select the most inclusion-free garnet fragments. As it was unfortunately not possible during hand-picking to distinguish whether a single garnet fragment belonged to a core or to a rim (there was no discernible difference in colour or texture, despite the garnet being chemically zoned most notably in HREEs), the separated garnet fragments were arbitrarily split into two fractions (grt-1: 54.9 mg; grt-2: 73.5 mg), assuming that each fraction would contain similar, but not identical, trace element abundances. A whole-rock powder of sample KP11-588 (w.r.: 92.2 mg), prepared in a tungsten carbide mill at RHUL, was also analysed in order to calculate garnet ages.

Analytical procedures

The methods for sample preparation and analysis largely followed those of Anczkiewicz & Thirlwall (2003) and Bird *et al.* (2013). The REE zoning profiles (Fig. 12) were used to estimate the approximate abundances of Sm, Nd, Lu, and Hf in the garnet cores in order to calculate the optimum Lu/Hf and Sm/Nd spike weights. These spikes were added to the samples prior to full dissolution in HF and HNO_3.

The samples were spiked, leached, and dissolved following the procedures outlined by Anczkiewicz & Thirlwall (2003), although in this instance H_2SO_4 leaching was not performed due to the scarcity of phosphate inclusions within the garnet (small monazite grains, which are relatively scarce, are the only phosphate inclusions). The samples were passed through Bio-Rad AG 50W-X8 cation resin to remove sequentially the high field strength elements (HFSEs), the LREEs, and the HREEs. Eichrom LN resin was used subsequently to separate Lu, Hf, Sm, and Nd from the different fractions collected from the cation columns. These final solutions were analysed by the GV IsoProbe MC-ICP-MS system at RHUL, using procedures outlined by Anczkiewicz & Thirlwall (2003). Isochron ages were calculated using IsoPlot v. 2.47 (Ludwig 2003) using decay constants of 1.865×10^{-11} yr^{-1} for ^{176}Lu (Scherer *et al.* 2001) and 6.54×10^{-12} yr^{-1} for ^{147}Sm (Lugmair & Marti 1978). In addition, two Nd samples were analysed on the IsotopX Phoenix thermal ionization mass spectrometer (TIMS) at RHUL, to confirm the small variations in Nd isotopic compositions.

Lu–Hf and Sm–Nd geochronology results

Garnets analysed from UHT granulite sample KP11-588 yielded precise Lu–Hf ages of 138.6 ± 0.7 Ma and 137 ± 0.6 Ma calculated for grt-1 and grt-2 fractions and the whole rock (i.e., 2-point isochrons), respectively (Fig. 17a; Table 5).

The Sm–Nd age is poorly constrained due to LREE-rich inclusions dominating the Nd budget of the analysed garnet, resulting in very small differences in measured $^{143}Nd/^{144}Nd$ ratios between the garnet and whole rock. It was not possible to construct a meaningful 3-point isochron (Fig. 17b). Sm–Nd ages calculated individually from grt-1 and grt-2 fractions are 6.0 ± 14.0 Ma and 7.1 ± 9.8 Ma, respectively (Table 6), together describing an imprecise 0–20 Ma age. Using instead the higher-precision IsotopX Phoenix TIMS $^{143}Nd/^{144}Nd$ ratio of 0.512067 ± 0.000004 for the grt-2 fraction, a Sm–Nd age of 10.6 ± 7.7 Ma is calculated (Fig. 17b). The same age is calculated also for a 3-point isochron using this result. These Sm–Nd results are permissive of a broadly "Neogene" date, consistent with that inferred for UHT metamorphism of the sample.

Lu mass balance

Lu and Hf contents determined by isotope dilution (ID) for the garnet fractions were around 5.2 and 0.34 ppm, respectively (Table 5). The Hf content is similar to that determined *in situ* on the garnet by LA-ICP-MS, indicating that it is unaffected by dissolution of inclusions such as zircon. However, the Lu content is substantially less than that measured by LA-ICP-MS in the garnet core, which is 10–35ppm (mean ca. 25ppm), suggesting that the garnet separates analysed for Lu–Hf are about 20% derived from the core, and 80% derived from the low-Lu rim. Since the Lu contents of the two garnet fractions analysed are only 0.5% different, they each represent very similar proportions of core and rim. Sm and Nd contents determined by ID were around 7 and 17 ppm respectively. The Sm is comparable to that measured by LA-ICP-MS, but the ID Nd content is 5–7× higher, suggesting that LREE-rich inclusions have contributed substantially to the REE budget of the garnet separates, despite being uncommon.

Synthesis

Several geochronological (zircon and monazite U–Pb, garnet Lu–Hf and Sm–Nd, and biotite $^{40}Ar/^{39}Ar$; Fig. 18), microchemical (REE analysis of zircon and garnet), and thermobarometry techniques (Ti-in-zircon; Zr-in-rutile; phase equilibria modelling) have now been applied to the residual UHT granulites of the Kobipoto Complex exposed in central Seram. To summarize these findings (new results are marked by an *):

- The protolith to the Kobipoto Complex was sourced, in part, from the Archean cratons of Western Australia, and was deposited in the Late Triassic (C_d zircon U–Pb ages between 3.4 Ga and 216 Ma; Pownall *et al.* 2017*a*; Fig. 5);
- There were two subsequent zircon crystallisation events: at *c.* 200 Ma (R_2), and at *c.* 16 Ma (R_m) (Pownall *et al.* 2014, 2017*a*);
- *The *c.* 200 Ma R_2 zircon crystallized at ~700˚C (Ti-in-zircon thermometry; Fig. 15) and probably grew during a metamorphic event (Th/U < 1; Fig. 14) *not* in equilibrium with garnet (as R_2 HREEs > 10× garnet HREEs; Fig. 13);
- *The *c.* 16 Ma R_m zircon crystallized at ~600˚C (Ti-in-zircon thermometry; Fig. 15) during a metamorphic event (Th/U < 1; Fig. 14) in an environment where garnet was present (as R_m HREEs ~ garnet HREEs; Fig. 13); *however*,
- *Zircons occurring as inclusions within garnet *did not* grow *c.* 16 Ma R_m rims (Fig. 9b–e);
- $^{40}Ar/^{39}Ar$ furnace step heating geochronology of biotite yielded an age of 16.34 ± 0.04 Ma, which is within uncertainty of the respective U–Pb (R_m) zircon age for the same sample (Fig. 18; Pownall *et al.* 2014, 2017*b*);
- *Monazite grains within the leucosome and included in garnet (re-)crystallized at *c.* 16 Ma and do not record an older history (Fig. 10);

- *Rutile grains in the leucosome must have crystallized under UHT conditions (~900˚C Zr-in-rutile *T*s), but rutile grains included within garnet yielded lower Zr-in-rutile temperatures of 600–750˚C (Fig. 16);
- *Most of the garnet grew as a peritectic phase, as evidenced by the occurrence of melt inclusions (Fig. 7);
- Major element zonation profiles of garnet are flat in the central region (Pownall 2015) and show evidence for resorption close to the rim (Fig. 11); *however*,
- *REE zonation profiles preserve evidence for distinct core and rim domains (Fig. 12);
- *The cores show large elevation in REE abundances (> 10× that of the rims) but are relatively small, accounting for < 9 vol.% of total garnet;
- *The garnet yielded precise Lu–Hf ages of 138.6 ± 0.7 and 137.9 ± 0.6 Ma for the two garnet separates (Fig. 17). Based on Lu mass balance, the analysed garnet is about 80% derived from the rim and 20% derived from the core.
- *The garnet yielded a Sm–Nd age of 10.6 ± 7.7 Ma, which is compromised by the large contribution of LREE-rich inclusions to the dissolved garnet Nd budget (Fig. 17).

Below is a discussion of what these results might mean for the metamorphic evolution of the Kobipoto Complex granulites:

What did the zircon record?

Since zircon may crystallize from a melt that is generated during anatexis (e.g. Schaltegger *et al.* 1999; Vavra *et al.* 1999), be modified by solid-state recrystallisation (e.g. Hoskin & Black 2000), form by subsolidus metamorphic reactions in response to Zr liberation (e.g. Fraser *et al.* 1997; Degeling *et al.* 2001), or may precipitate from metamorphic or metasomatic fluids across a broad range of temperatures (e.g. Rubatto & Hermann 2003; Hay & Dempster 2009), it is far from straightforward to assign U–Pb zircon ages to a particular event (Harley *et al.* 2007). Furthermore, metamorphic-attributed U–Pb ages are unlikely to date peak *P–T* conditions (e.g., Roberts & Finger 1997; Tedeschi *et al.* 2017) but rather an episode of zircon growth facilitated by Zr-rich metamorphic fluids or solid-state Zr diffusion during metamorphic reactions. Closely-matched rare earth element (REE) patterns between the zircon and metamorphic minerals suspected to have coexisted with the zircon under equilibrium conditions are considered by many as the best evidence for identifying 'metamorphic zircon' (e.g. Hokada & Harley 2004; Rubatto & Hermann 2007*a*, *b*; Harley *et al.* 2007). Additional evidence may come from Th/U zircon ratios, since metamorphic zircon commonly has Th/U ratios < 0.1, and magmatic zircon > 0.1 (Rubatto 2002). However, there are numerous examples, particularly from metaluminous rocks, of metamorphic zircon with Th/U ratios that do not match this criterion (e.g. Vavra *et al.* 1999; Rubatto 2017), and very low Th/U ratios (i.e. < 0.01) may instead relate to zircon formed by low-*T* metasomatism (Harley *et al.* 2007).

***c*. 16 Ma R_m zircon.** R_m zircon rims have very similar HREE abundances to garnet analysed from sample KP11-588, with garnet core and rim abundances neatly bracketing the entire range of R_m zircon HREE profiles (Fig. 13). This provides strong evidence for the *c*. 16 Ma R_m zircon having grown in the presence of this garnet, most probably from Zr liberated by consumption of the garnet rims (cf. Degeling *et al.* 2001; Sajeev *et al.* 2010). A metamorphic origin is further supported by U/Pb ratios that are consistently < 0.1 (Fig. 14).

As discussed by Pownall (2015), it is unlikely that the 16 Ma zircon (and, for similar reasons, the 16 Ma monazite) date the peak of metamorphism (cf. Kohn *et al.* 2015; Yakymchuk & Brown 2014), but instead a point on the *P–T* path that has passed through UHT conditions. Zircon growth can only occur if sufficient free Zr is available, so if Zr-bearing minerals, such as garnet, were consumed, Zr would have been liberated and zircon growth enabled or promoted (*cf.* Degeling *et al.*

2001). The retrograde history of the Kobipoto Complex UHT granulites is characterized by the replacement of garnet during reaction with sillimanite to form cordierite + spinel-dominated ordered reaction microstructures, and zircons located in this microtextural setting crystallized R_m rims. As noted by Sajeev *et al.* (2010), the formation of cordierite from garnet in the presence of melt would have released Zr that would have promoted zircon growth (cf. Fraser *et al.* 2000; Degeling *et al.* 2001). We therefore interpret that the *c*. 16 Ma R_m zircon rims were produced by post-peak metamorphic reactions that also produced the cordierite coronae and cordierite-spinel symplectites (Fig. 3e). This would have occurred during near-isothermal retrogression, after the metamorphic peak, and below 6 kbar pressure – the lower-*P* limit of garnet stability (Fig. 4). Ti-in-zircon thermometry would pinpoint the R_m zircon crystallisation temperature at ~600˚C (Fig. 15), although THERMOCALC Ave*PT* thermometry yielded slightly hotter (754 ± 116˚C at 4.0 ± 1.0 kbar) conditions for the post-peak reaction microstructures (Pownall 2015). Despite not having dated peak metamorphism, the complex's rapid exhumation and cooling history inferred from $^{40}Ar/^{39}Ar$ geochronology (Pownall *et al.* 2014, 2017*b*) would mean that R_m zircon crystallisation occurred very shortly afterwards.

Interestingly, zircon grains included in garnet did not grow R_m rims (Fig. 9) and so did not record *c*. 16 Ma ages. These zircons experienced the entire UHT metamorphic event without being affected by it, presumably because they were isolated from Zr^{4+} liberated by garnet rim breakdown after the metamorphic peak. We therefore infer that the ~30% of grains from sample KP11-588 mounted for SHRIMP U–Pb dating that do not feature R_m rims were separated from within garnet, and the rest from post-peak reaction microstructures and the leucosome.

Despite not having formed under UHT conditions, the R_m zircon rims have several characteristics in common with zircons interpreted to have formed under UHT metamorphic conditions in different terranes (e.g., Santosh *et al.* 2007; Sajeev *et al.* 2010; Kusiak *et al.* 2013). These 'UHT zircons' are reported typically as being U-rich (CL dark) and poorly-zoned with low Th/U ratios. Santosh *et al.* (2007) proposed that an increase in metamorphic temperature progressively destroys the oscillatory zoning, leaving the zircon uniformly dark in CL. Sajeev *et al.* (2010) attributed poorly-zoned zircon overgrowths with low Th/U ratios and similar low CL response from Sri Lankan granulites to UHT metamorphism at *c*. 550 Ma. Similarly, Kusiak *et al.* (2013) described CL-dark low-Th, high-U UHT zircon from the Napier Complex, Antarctica. We demonstrate here the possibility that 'UHT zircon' matching the same chemistry and texture may also form at much lower temperatures after the UHT metamorphic peak.

***c*. 200 Ma R_2 zircon.** R_2 zircon zones have HREE abundances at least an order of magnitude higher than R_m zircon rims and the garnet (Fig. 13). For this reason, it is unlikely that they grew during the most recent episode of garnet crystallisation related to the UHT metamorphism. They must have instead grown during an earlier event. Ti-in-zircon temperatures of ~700˚C and relatively low U/Th ratios (mostly <0.1) together suggest a metamorphic origin for the zircon at around upper-amphibolite grade. As R_2 zircon formed, in part, by recrystallisation of the detrital cores (Pownall *et al.* 2017*a*), growth was likely in the presence of ample fluid/melt. There is also a possibility that this R_2 zircon grew contemporaneously with an early episode of garnet growth, or at least during the same Late Triassic–Early Jurassic orogenic event in which garnet also formed, as discussed later.

These results further support the interpretation of an upper-amphibolite facies metamorphic event having affected the NW Australian margin in the Late Triassic–Early Jurassic (Pownall *et al.* 2017*a*). According to tectonic reconstructions by Hall (2012), this metamorphic event would shortly predate rifting of the Banda and Argo blocks from the NW Australia the subsequent opening of the Proto-Banda sea in the Middle Jurassic.

What did the monazite record?

Monazite grains dated *in situ* from the leucosome and from within garnet gave ages of 16.4 ± 0.4 Ma (Fig. 10) – identical, within uncertainty, to the R_m zircon. We therefore interpret the monazite to have similarly dated a point on the high-temperature decompression path after the peak of UHT metamorphism and in the presence of melt. As the monazite inclusion dated in this study is located close to leucosome in the margin of the garnet and also connected to a fracture network (Fig. 6d), it may have been recrystallized by circulating fluids shortly post-dating the UHT event (*cf*. Williams *et al.* 2011; Kelly *et al.* 2012; Taylor *et al.* 2014). R_2 zircon inclusions within garnet were evidently more resilient to any fluid-mediated resetting effect.

What do the Zr-in-rutile temperatures mean?

Rutile grains from the leucosome (Fig. 6f) recorded Zr-in-rutile temperatures (Tomkins *et al.* 2007) as high as 907 ± 14˚C, whereas rutile grains included in garnet (Fig. 6e) recorded temperatures between ~600–750˚C (Fig. 16). In the leucosome, it is reasonable to assume an $aSiO_2$ of 1 and unimpeded exchange of Zr^{4+} and Ti^{4+} between rutile and (R_m) zircon. We therefore consider this result to be reliable piece of further evidence that the Kobipoto Complex granulites were metamorphosed under UHT conditions.

The rutile grains within garnet must have also experienced the same peak temperature, but failed to record it. This is likely because the rutile and (R_2) zircon grains included within garnet on the prograde path were shielded from each other under peak conditions and were not able to equilibrate, prohibiting free $Zr^{4+} \fallingdotseq Ti^{4+}$ exchange. Failure of zircon grains within garnet to crystallize *c*. 16 Ma (R_m) rims further demonstrates that Zr^{4+} from the leucosome did not pass into garnet. The broad spread in rutile Zr contents may therefore reflect the different temperatures (~600–750˚C) rutile grains were included by the garnet during its prograde growth.

What do the 138 Ma Lu–Hf garnet ages mean?

The 138.6 ± 0.7 and 137.9 ± 0.6 Ma Lu–Hf garnet ages (Fig. 17a) are at first puzzling because an Early Cretaceous metamorphic or magmatic episode has never before been reported for Australian-affinity crust in east Indonesia. Previous work indicates a period of tectonic and magmatic quiescence in the northwest Australian margin at this time (e.g. Audley-Charles *et al.* 1988; Fraser *et al.* 1993; Hall 2012). A *c*. 143 Ma metamorphic episode has been documented in western Borneo, but *not* from a part of Borneo that was derived from Australia (Breitfeld *et al.* 2017). Given also that, for the *same sample* (*i*) this 138 Ma Lu–Hf garnet age does not correlate even closely with zircon or monazite crystallisation events, (*ii*) garnet HREE abundances equilibrated with those in 16 Ma zircon (Fig. 13), and (*iii*) the respective Sm–Nd garnet age is significantly younger (10.6 ± 7.7 Ma, although imprecise), we do not think that this Cretaceous Lu–Hf age can date a real metamorphic or magmatic event. We argue below that this age is the result of mixing between *c*. 200 Ma garnet cores with *c*. 16 Ma garnet rims. In order that ^{176}Hf produced during the *c*. 200 Ma event was not lost from the garnet by diffusion during UHT metamorphism at *c.* 16 Ma, we further argue that duration of the UHT metamorphism must have been very short.

The Kobipoto Complex garnets retain evidence in their HREE zonation for two separate episodes of garnet growth (Fig. 12) despite having relatively flat major element profiles (Fig. 11). Hf and Lu concentrations are 3× and 30× higher, respectively, in garnet cores compared to the rims. On the other hand, Sm and Nd concentrations are more uniform and do not features a sharp core–rim transition. Furthermore, the Lu–Hf garnet ages of 137.9 ± 0.6 and 138.6 ± 0.7 Ma are significantly older that their respective 10.6 ± 7.7 Ma Sm–Nd age. Although it is common for Lu–Hf ages to be slightly older than Sm–Nd ages for the same garnet sample grown during a single metamorphic event (e.g. Anczkiewicz *et al.* 2007, 2012; Kylander-Clark *et al.* 2007; Bird *et al.* 2013; Smit *et al.* 2013; Yakymchuk *et al.* 2015), in this instance the discrepancy is far too large to be accounted for by any

systematic offset. A component of Hf^{4+}, but not Nd^{3+}, must have been derived from a previous metamorphic event, requiring that (*i*) part of the garnet is significantly older than the UHT metamorphism; and (*ii*) the UHT metamorphic event then remobilized major element and LREE cations (including Sm and Nd) without significantly redistributing the highly-retentive cations (including Lu and Hf).

These requirements are permitted by the different Lu–Hf and Sm–Nd closure temperatures and Lu^{3+} and Hf^{4+} diffusion behaviours in garnet. According to Smit *et al.* (2013), for rapid cooling rates (> 100 ˚C Ma^{-1}) and a garnet diffusion domain radius of 1 mm, the closure temperature of both Sm–Nd and Lu–Hf systems would be approximately > 850˚C and > 1000˚C, respectively. Furthermore, Bloch *et al.* (2015, p. 16) determined that Hf^{4+} (and Lu^{3+}) are only able to fully homogenize when "unusually long periods of metamorphism persist", or when very high temperatures (i.e., >> 900˚C) are attained. For instance, a 1 mm-diameter garnet may take *c.* 12 myr at 900˚C, but *c.* 250 myr at 800˚C, to fully homogenize its Hf (Bloch *et al.* 2015, p. 16, fig. 12). The fact that HREE zoning is preserved in garnet (Fig. 13) and that UHT metamorphism did not 'reset' the Lu–Hf clock indicates that the duration of UHT metamorphism must have been short (i.e., significantly less than 12 myr – perhaps just a few myr).

The metamorphic event recorded by the R_2 zircon between 215–173 Ma is the only known candidate for producing an older generation of garnet from which this older Hf might have been sourced. As such, we propose that the garnet cores formed during the previously-identified Late Triassic–Early Jurassic amphibolite-facies metamorphic event. It might be expected that HREE concentrations of garnet cores and R_2 zircon should be similar, if it is assumed that these two minerals grew in equilibrium. However, while not opened to complete diffusion, a slight depletion in garnet core HREE concentration may still have occurred during the UHT event. This is one possible explanation why garnet core HREE concentrations are lower than those of R_2 zircon (Fig. 13). An alternative explanation is that R_2 zircon and garnet grew during different stages of the same orogenic event and/or formed in different domains, and so never had similar HREE abundances.

Lu–Hf garnet mixing model. In order to test the viability of this idea, we performed a simple mixing calculation using values approximated from the LA-ICP-MS core–rim traverses (Fig. 12) of Lu_{core} / Lu_{rim} = 25 ppm / 1 ppm = 25 and Hf_{core} / Hf_{rim} = 0.34 ppm / 0.05 ppm = 6.80, and using the whole rock data shown in Table 5. The core age was fixed at 200 Ma and the rim age fixed at 16 Ma by rotating manually the slope of the model isochrons about the whole rock $^{176}Hf/^{177}Hf$ and $^{176}Lu/^{177}Hf$ ratios. Then, cores and rims were then mixed in a 20_{core}:80_{rim} ratio, as determined from the Lu mass balance (discussed previously). This produced a mixed model age of 131.3 Ma. However, this model age is very sensitive to the Hf_{core} / Hf_{rim} ratio, which cannot be determined accurately from the available LA-ICP-MS traverses. Taking lower and upper estimates for Hf_{core} / Hf_{rim} of 4.9 (using instead 0.07 ppm Hf_{rim}) and 11.3 (using instead 0.03 ppm Hf_{rim}) yielded model mixing ages between 116.5 and 151.2 Ma (Fig. 17c). The actual Lu–Hf ages of 137.9 ± 0.6 and 138.6 ± 0.7 Ma fall squarely between these limits. Therefore, we demonstrate it entirely plausible that the *c*. 138 Ma Lu–Hf ages were produced by mixing between *c*. 200 Ma cores (20% contribution) and *c*. 16 Ma rims (80% contribution).

Although a smaller component of the mixed age, the *c*. 200 Ma cores have far higher Lu and Hf concentrations than the *c.* 16 Ma rims (Fig. 12), and so affected the age to a greater extent. Also, since Lu^{3+} diffusion is around 10 times faster than Hf^{4+} diffusion (e.g., Kohn 2009; Anczkiewicz *et al.* 2012; Baxter & Scherer 2013), partial HREE retention may have lowered residual $^{176}Lu/^{177}Hf$ ratios, further skewing Lu–Hf ages towards older values (up until the point all Hf^{4+} and Lu^{3+} are lost and the age is reset). This issue of Hf inheritance from previous garnet growth events has been described previously as resulting in systematically older Lu–Hf ages (Bloch & Ganguly 2015; Raimondo *et al.* 2017). Counter to this, garnet resorption, which has affected the garnets of the

Koibpoto Complex granulites to a large extent, may have resulted in a younging of the Lu–Hf age as Lu^{3+} is preferentially retained over Hf^{4+} in the resorbed portion of the garnet (Kelly *et al*. 2011).

Summary

In summary, we interpret UHT metamorphism and melting on Seram occurred just prior to 16 Ma, and an upper-amphibolite facies metamorphic event occurred during the Triassic/Jurassic (*c*. 200 Ma), for the following reasons: (*i*) the HREE abundances in garnet (a major constituent of the peak UHT metamorphic assemblage) tightly bracket those in the 16 Ma zircon, whereas 200 Ma zircon HREE abundances are 10× higher (Fig. 13); (*ii*) monazite included within garnet yielded a $^{206}Pb/^{238}U$ age of 16.4 ± 0.4 Ma (Fig. 10) – within uncertainty of those ages from zircon (Fig. 18); (*iii*) Th/U ratios for the *c*. 16 Ma R_m zircon are consistently below 0.1, consistent with a metamorphic origin (Fig. 14); (*iv*) Garnet yielded a Sm–Nd age of 10.6 ± 7.7 Ma, within uncertainty of *c*. 16 Ma zircon; (*v*) Garnet Lu–Hf ages of *c*. 138 Ma are explained by mixing between *c*. 200 Ma cores with *c.* 16 Ma rims (Fig. 17c); (*vi*) rutile present in the leucosome records Zr-in-rutile temperatures > 900˚C (Fig. 16); (*vii*) Multiple $^{40}Ar/^{39}Ar$ ages (Pownall *et al.* 2017*b*) also document a regionally-significant metamorphic event that affected Seram's Tehoru Formation at 16 Ma; (*viii*) A 17 Ma $^{40}Ar/^{39}Ar$ age from phlogopite in a lamprophyric dyke intruding the Kobipoto Complex lherzolite demonstrates the presence of hot mantle rocks at that time, necessary to have achieved UHT conditions (Pownall *et al.* 2017*b*); and (*ix*) tectonic reconstructions at *c*. 16 Ma indicate a marked change in the tectonic environment in the Banda region, as the Banda slab began to subduct with rollback of the subduction hinge ESE into the Banda Embayment (Fig. 19), driving regional extension (Spakman & Hall 2010; Hall 2011, 2018). These multiple lines of evidence add further support to the interpretation that the Seram granulites recorded Earth's youngest-known episode of UHT crustal metamorphism in response to rollback-driven mantle exhumation (Pownall *et al*. 2014, 2017*a*).

We further propose that garnet cores grew at *c*. 200 Ma, during the same orogenic event that caused R_2 zircon crystallisation. During the Miocene UHT event, prograde garnet rims overgrew these older cores. The major elements later equilibrated between the two different generations during peak conditions, erasing any zoning. Upon rapid cooling and decompression from UHT conditions, garnets cooled through the Sm–Nd closure temperature (consistent with the Sm–Nd age being equal to or less than the zircon and monazite U–Pb ages), but the garnet was never hot enough for long enough to have been 'opened' to appreciable Hf^{4+} diffusion. Consequently, the thermal pulse that drove UHT metamorphism must have been short (Pownall *et al.* 2014; Pownall 2015) and failed to enable complete outward diffusion of Hf^{4+} accumulated in the *c*. 200 Ma garnet cores. These "fast" granulites (Harley 2016) cannot have existed above 900˚C much longer than a few million years before being exhumed very rapidly, as supported also by the identical-within-uncertainty biotite $^{40}Ar/^{39}Ar$ (Pownall *et al.* 2017*b*), zircon U–Pb, and monazite U–Pb ages (Fig. 18).

Conclusions

Metamorphic evolution of the Kobipoto Complex UHT granulites

1) The pelitic protolith to the Kobipoto Complex granulites was deposited by 216 Ma. Detrital zircons (C_d) as old as 3.4 Ga confirm this material was derived, in part, from the western Australian cratons (Fig. 19a).
2) The protolith to the Kobipoto Complex was metamorphosed in the upper-amphibolite facies (± partial melting) between 215 and 173 Ma as recorded by R_2 zircon rims that partially recrystallized older C_d cores (evidenced by ~700˚C Ti-in-[R_2]zircon temperatures and Th/U < 0.1). Small garnets with high HREE contents also likely grew during this Late Jurassic–

Early Cretaceous event, in order to account for elevated ^{176}Hf contents that cannot be explained by a single garnet growth event at *c*. 16 Ma. It is possible that more than one metamorphic–magmatic episode occurred between 215 and 173 Ma which shortly predated the rifting of adjacent continental blocks from the NW Australian margin (Fig. 19b).

3) Prograde metamorphism preceding the UHT peak was not recorded by the investigated geochronometers, but must have occurred between 23 Ma (the initial Australia–SE Asia collision age; Hall 2011) and 16 Ma (growth of retrograde R_m zircon and monazite). Garnet growth, principally as a peritectic product (evidenced by melt inclusions) engulfed many C_d+R_2 zircon grains and some rutile and monazite grains (Fig. 19d). The zircons, after their inclusion in garnet, did not crystallize new rims. Rutile grains, after their inclusion, did not adjust their Zr contents, recording collectively a spread of different Zr-in-rutile temperatures (600–750˚C) along the prograde path.
4) Hot leucosome must have been present at the peak of UHT metamorphism (925˚C and 9 kbar; Pownall 2015). Rutile grains within the leucosome, adjacent to garnet, recorded Zr-in-rutile temperatures of ~900˚C through exchange of Zr^{4+} and Ti^{4+} with zircon grains present also in the leucosome (Fig. 19d). At this time, garnet comprized a modelled 30 vol% of the rock (Pownall 2015). As the garnets no longer preserve major element or LREE core–rim zoning, in contrast to the more retentive HREEs, it is likely that these less retentive cations were homogenized under peak conditions. Diffusion of HREEs from core to rim may have occurred to a small extent, since R_2 zircon which grew contemporaneously with the garnet cores at *c*. 200 Ma have higher HREE abundances.
5) During the granulites' post-peak evolution, garnet reacted with sillimanite to form the cordierite and spinel-rich coronae. At *c*. 16 Ma, as the rock was exhumed above ~ 20 km depth (~ 6 kbar), garnet no longer remained part of the equilibrium assemblage. Zr^{4+} liberated by metamorphic reactions consuming the outermost garnet rims drove crystallisation of *c*. 16 Ma R_m rims on zircon grains in the leucosome and on zircons now located in cordierite + spinel post-peak reaction microstructures (Fig. 19e). Ti-in-[R_m]zircon temperatures of just 600˚C attest to the late crystallisation of zircon in the UHT granulites' retrograde history.
6) The 138.6 ± 0.7 and 137.9 ± 0.6 Ma garnet Lu–Hf ages do not correlate to any known geological event in the Banda region (Fig. 19c). We interpret these ages to be the product of mixing between *c*. 200 Ma garnet cores (~20% contribution) and *c*. 16 Ma garnet rims (~80% contribution) (Fig. 17c, 19e). The garnet Sm–Nd age of 10.6 ± 7.7 Ma is imprecise, but most probably records initial cooling from the UHT metamorphic peak at *c*. 16 Ma. Unlike Hf, there is no evidence that Nd produced within c. 200 Ma garnet cores was retained in garnet during Miocene UHT metamorphism. In order that the Lu–Hf 'clock' was not reset by the UHT metamorphism, the granulites cannot have resided under UHT conditions for longer than a few million years.

Broader implications

1) Zircon grains in shielded microtextural sites (in this instance as inclusions within garnet) may be subjected to an entire UHT metamorphic cycle *without* crystallizing new rims, and therefore *without* recording the UHT event.
2) Short-lived UHT metamorphic events are sometimes unable to reset the Lu–Hf system in garnet. In such instances, Hf retention from a previous metamorphic event may lead to a mixed Lu–Hf age even for garnets that no longer preserve major element zonation.
3) Rather than having formed within a large, long-lived, hot collisional orogen—the most common explanation for UHT rocks discovered in Proterozoic terranes—these Indonesian

Miocene granulites record a history of short-lived UHT metamorphism and subsequent rapid exhumation.

Acknowledgements

Many thanks to Yasinto Priastomo, Ramadhan Adhitama, and Adianto Trihatmojo (Institut Teknologi Bandung) for assistance during the fieldwork that made this study possible. Thanks also to Juliane Hennig for assistance with garnet dating, James Tolley for assistance with the RSES LA-ICP-MS system, Melanie Sieber for helping to acquire the *in situ* CL images of zircon grains, and Antonio Acosta-Vigil for encouraging me to search for melt inclusions. This paper benefitted greatly from insightful reviews by Chris Yakymchuk, the editorship of Pierre Lanari, and discussions with Anna Bird and Steph Walker.

Funding information

This research was funded by the SE Asia Research Group (Royal Holloway University of London) and Australian Research Council (ARC) DECRA fellowship DE160100128 awarded to J.M.P.

References

Aleinikoff, J.N., Schenck, W.S., Plank, M.O., Srogi, L., Fanning, C.M., Kamo, S.L., Bosbyshell, H., 2006. Deciphering igneous and metamorphic events in high-grade rocks of the Wilmington Complex, Delaware: Morphology, cathodoluminescence and backscattered electron zoning, and SHRIMP U-Pb geochronology of zircon and monazite. GSA Bulletin 118, 39–64. doi:10.1130/B25659.1

Anczkiewicz, R., Thirlwall, M.F., 2003. Improving precision of Sm-Nd garnet dating by H_2SO_4 leaching: a simple solution to the phosphate inclusion problem, *in*: Vance, D., Müller, W., Villa, I.M. (Eds.), Geochronology: Linking the Isotope Record with Petrology and Textures. Geological Society, London, Special Publications 220, 83–91.

Anczkiewicz, R., Mazur, S., Szczepanski, J., Storey, C., Crowley, Q., Villa, I.M., Thirlwall, M.F., Jeffries, T.E., 2007. Lu–Hf geochronology and trace element distribution in garnet: Implications for uplift and exhumation of ultra-high pressure granulites in the Sudetes, SW Poland. Lithos 95, 363–380.

Anczkiewicz, R., Thirlwall, M.F., Alard, O., Rogers, N.W., Clark C., 2012. Diffusional homogenization of light REE in garnet from the Day Nui Con Voi Massif in N-Vietnam: Implications for Sm–Nd geochronology and timing of metamorphism in the Red River shear zone. Chemical Geology 318–319, 16–30.

Audley-Charles, M.G., 1988. Evolution of the southern margin of Tethys (North Australian region) from early Permian to late Cretaceous, *in*: Audley-Charles, M.G., and Hallam, A. (Eds.), Gondwana and Tethys. Geological Society, London, Special Publications 37, 79–100.

Baxter, E.F. & Scherer, E.E., 2013. Garnet geochronology: Timekeeper of tectonometamorphic processes, Elements 9, 433–438.

Bird, A.F., Thirlwall, M.F., Strachan, R.A., Manning, C.J., 2013. Lu–Hf and Sm–Nd dating of metamorphic garnet: evidence for multiple accretion events during the Caledonian orogeny in Scotland. Journal of the Geological Society 170, 301–317.

Bloch, E., Ganguly, J., 2015. ^{176}Lu–^{176}Hf geochronology of garnet II: numerical simulations of the development of garnet–whole-rock ^{176}Lu–^{176}Hf isochrons and a new method for constraining

the thermal history of metamorphic rocks. Contributions to Mineralogy and Petrology 169, 14, doi: 10.1007/s00410-015-1115-x.
Bloch, E., Ganguly, J., Hervig, R. & Cheng, W., 2015. ^{176}Lu–^{176}Hf geochronology of garnet I: experimental determination of the diffusion kinetics of Lu^{3+} and Hf^{4+} in garnet, closure temperatures and geochronological implications. Contributions to Mineralogy and Petrology 169, 12, doi: 10.1007/s00410-015-1109-8.
Bowin, C., Purdy, G.M., Johnston, C., Shor, G., Lawyer, L., Hartono, H., Jezek, P., 1980. Arc-continent collision in the Banda Sea region. AAPG Bulletin 64, 868–915.
Breitfeld, H.T., Hall, R., Galin, T., Forster, M.A., BouDagher-Fadel, M.K., 2017. A Triassic to Cretaceous Sundaland–Pacific subduction margin in West Sarawak, Borneo. Tectonophysics 694, 35–56.
Brown, M., 2006. Duality of thermal regimes is the distinctive characteristic of plate tectonics since the Neoarchean. Geology 34, 961–964.
Brown, M., 2014. The contribution of metamorphic petrology to understanding lithosphere evolution and geodynamics. Geoscience Frontiers 5, 553–569.
Cesare, B., Acosta-Vigil, A., Bartoli, O., and Ferrero, S., 2015. What can we learn from melt inclusions in migmatites and granulites? Lithos 239, 186–216.
Charlton, T.R., Kaye, S.J., Samodra, H., Sardjono, 1991. Geology of the Kai Islands: implications for the evolution of the Aru Trough and Weber Basin, Banda Arc, Indonesia. Marine and Petroleum Geology 8, 62–69. doi:10.1016/0264-8172(91)90045-3
Degeling, H., Eggins, S., Ellis, D.J., 2001. Zr budgets for metamorphic reactions, and the formation of zircon from garnet breakdown. Mineralogical Magazine 65, 749–758.
Ely, K.S., Sandiford, M., Phillips, D., Boger, S.D., 2014. Detrital zircon U–Pb and $^{40}Ar/^{39}Ar$ hornblende ages from the Aileu Complex, Timor-Leste: provenance and metamorphic cooling history. Journal of the Geological Society 171, 299–309. doi:10.1144/jgs2012-065
Ferry, J.M., Watson, E.B., 2007. New thermodynamic models and revised calibrations for the Ti-in-zircon and Zr-in-rutile thermometers. Contributions to Mineralogy and Petrology 154, 429–437. doi:10.1007/s00410-007-0201-0
Fraser, T.H., Bon, J. & Samuel, L. 1993. A new dynamic Mesozoic stratigraphy for the West Irian micro-continent Indonesia and its implications. Indonesian Petroleum Association, Proceedings 22nd Annual Convention, 707-761.
Fraser, G., Ellis, D., Eggins, S., 1997. Zirconium abundance in granulite-facies minerals, with implications for zircon geochronology in high-grade rocks. Geology 25, 607–610. doi:10.1130/0091-7613(1997)025<0607:ZAIGFM>2.3.CO;2
Gafoer, S., Suwitodirdjo, K., and Suharsono, 1993. Geological map of the Bula and Watubela sheet, Maluku, 1:250000, Geological Research and Development Centre, Bandung, Indonesia.
Germeraad, J.H., 1946. Geology of central Seran, *in*: Rutten, L., Hotz, W. (Eds.), Geological, Petrographical, and Palaeontological Results of Explorations, Carried Out From September 1917 Till June 1919 in the Island of Ceram. De Bussy, Amsterdam, p. 135.
Hall, R., 2011. Australia–SE Asia collision: plate tectonics and crustal flow, *in*: Hall, R., Cottam, M.A., Wilson, M.E.J. (Eds.), The SE Asian Gateway: History and Tectonics of the Australia-Asia Collision. Geological Society, London, Special Publications 355, 75–109. doi:10.1144/SP355.5
Hall, R., 2012. Late Jurassic–Cenozoic reconstructions of the Indonesian region and the Indian Ocean. Tectonophysics 570-571, 1–41. doi:10.1016/j.tecto.2012.04.021
Hall, R., 2017. Southeast Asia: New views of the geology of the Malay Archipelago. Annual Review of Earth and Planetary Sciences 45, 331–358.
Hall, R., 2018. The subduction initiation stage of the Wilson Cycle, *in*: Wilson, R.W., Houseman, G.A., McCaffrey, K.J.W., Doré, A.G., Buiter, S.J.H. (Eds.), Fifty Years of the Wilson Cycle

Concept in Plate Tectonics. Geological Society, London, Special Publications 470. doi:10.1144/SP470.3
Hall, R., Patria, A., Adhitama, R., Pownall, J.M., White, L.T., 2017. Seram, the Seram Trough, the Aru Trough, the Tanimbar Trough and the Weber Deep: A new look at major structures in the eastern Banda Arc. Indonesian Petroleum Assoication, Proceedings 41, IPA17-91-G.
Hamilton, W., 1979. Tectonics of the Indonesian region. US Geological Survey Professional Paper 1078, 345 pp.
Harley, S.L., 2008. Refining the *P–T* records of UHT crustal metamorphism. Journal of Metamorphic Geology 26, 125–154.
Harley, S.L., 2016. A matter of time: The importance of the duration of UHT metamorphism. Journal of Mineralogical and Petrological Sciences 111, 50–72.
Harley, S.L., Kelly, N.M., Möller, A., 2007. Zircon Behaviour and the Thermal Histories of Mountain Chains. Elements 3, 25–30.
Hay, D.C., Dempster, T.J., 2009. Zircon Behaviour during Low-temperature Metamorphism. Journal of Petrology 50, 571–589. doi:10.1093/petrology/egp011
Hensen, B.J. & Green, D.H., 1971. Experimental study of the stability of cordierite and garnet in pelitic compositions at high pressures and temperatures: I. Compositions with excess alumino-silicate. Contributions to Mineralogy and Petrology 33, 309–330.
Hinschberger, F., Malod, J.-A., Réhault, J.-P., Dyment, J., Honthaas, C., Villeneuve, M., Burhanuddin, S., 2000. Origine et evolution du basin Nord-Banda (Indonésie): apport des données magnétiques. C.R. Acad. Sci., Ser. IIa: Sci. Terre Planets 331, 507–514.
Hinschberger, F., Malod, J.-A., Dyment, J., Honthaas, C., Réhault, J.-P., Burhanuddin, S., 2001. Magnetic lineations constraints for the back-arc opening of the Late Neogene South Banda Basin (eastern Indonesia). Tectonophysics 333, 47–59.
Hokada, T., Harley, S.L., 2004. Zircon growth in UHT leucosome: constraints from zircon-garnet rare earth element (REE) relations in Napier Complex, East Antarctica. Journal of Mineralogical and Petrological Sciences 99, 180–190.
Honthaas, C., Villeneuve, M., Réhault, J.-P., Bellon, H., Cornee, J.-J., Saint-Marc, P., Butterlin, J., Gravelle, M., Burhanuddin, S., 1997. L'île de Kur: géologie du flanc oriental du bassin de Weber (Indonésie orientale). Comptes Rendus de l'Académie des Sciences - Series IIA - Earth and Planetary Science 325, 883–890.
Honthaas, C., Maury, R.C., Priadi, B., Bellon, H., Cotten, J., 1999. The Plio–Quaternary Ambon arc, Eastern Indonesia. Tectonophysics 301, 261–281. doi:10.1016/S0040-1951(98)00227-3
Hoskin, P.W.O., Black, L.P., 2000. Metamorphic zircon formation by solid-state recrystallization of protolith igneous zircon. Journal of Metamorphic Geology 18, 423–439. doi:10.1046/j.1525-1314.2000.00266.x
Kelly, E.D., Carlson, W.D., Connelly, J.N., 2011. Implications of garnet resorption for the Lu–Hf garnet geochronometer: an example from the contact aureole of the Makhavinekh Lake Pluton, Labrador. Journal of Metamorphic Petrology 29, 901–916.
Kelly, N.M, Harley, S.L., Möller, A., 2012. Complexity in the behavior and recrystallization of monazite during high-T metamorphism and fluid infiltration. Chemical Geology 322–323, 192–208.
Kelsey, D.E., 2008. On ultrahigh-temperature metamorphism. Gondwana Research 13, 1–29.
Kelsey, D.E., Hand, M., 2015. On ultrahigh temperature crustal metamorphism: Phase equilibria, trace element thermometry, bulk composition, heat sources, timescales and tectonic settings. Geoscience Frontiers 6, 311–356.
Klompé, T.H.F., 1954. The structural importance of the Sula Spur (Indonesia). Indonesian Journal of Natural Sciences 110, 21–40.
Kohn, M.J., 2009. Models of garnet differential geochronology. Geochimica et Cosmochimica Acta 73, 170-182.

922 Kohn, M.J., Corrie, S.L., Markley, C., 2015. The fall and rise of metamorphic zircon. American
923 Mineralogist 100, 897–908.
924 Kusiak, M.A., Whitehouse, M.J., Wilde, S.A., Dunkley, D.J., Menneken, M., Nemchin, A.A., Clark,
925 C., 2013. Changes in zircon chemistry during Archean UHT metamorphism in the Napier
926 Complex, Antarctica. American Journal of Science 313, 933–967. doi:10.2475/09.2013.05
927 Kylander-Clark, A.R.C., Hacker, B.R., Johnson, C.M., Beard, B.L., Mahlen, N.J., Lapen, T.J., 2007.
928 Coupled Lu–Hf and Sm–Nd geochronology constrains prograde and exhumation histories of
929 high- and ultrahigh-pressure eclogites from western Norway. Chemical Geology 242, 137–154.
930 Linthout, K., Helmers, H., Sopaheluwakan, J., Nila, E.S., 1989. Metamorphic complexes in Buru and
931 Seram, Northern Banda Arc. Netherlands Journal of Sea Research 24, 345–356.
932 doi:10.1016/0077-7579(89)90160-9
933 Linthout, K., Helmers, H., Wijbrans, J.R., Van Wees, J.D.A.M., 1996. $^{40}Ar/^{39}Ar$ constraints on
934 obduction of the Seram ultramafic complex: consequences for the evolution of the southern
935 Banda Sea. Geological Society, London, Special Publications 106, 455–464.
936 doi:10.1144/GSL.SP.1996.106.01.28
937 Ludwig, K.R., 2003. Isoplot 3.0: A geochronological toolkit for Microsoft Excel. Berkeley
938 Geochronological Centre Special Publication 4.
939 Ludwig, K.R., 2009. SQUID 2: A user's manual. Berkeley Geochronological Centre Special
940 Publication 5.
941 Lugmair, G.W., Marti, K., 1978. Lunar initial $^{143}Nd/^{144}Nd$: differential evolution of the lunar crust
942 and mantle. Earth and Planetary Science Letters 39, 349–357.
943 McDonough, W.F., and Sun, S.-S., 1995. The composition of the Earth. Chemical Geology 120, 223–
944 253.
945 Müller, W., Shelley, M., Miller, P., Broude, S., 2009. Initial performance metrics of a new custom-
946 designed ArF excimer LA-ICPMS system coupled to a two-volume laser-ablation cell. Journal
947 of Analytical Atomic Spectrometry 24, 209–214.
948 Powell, R., Holland, T.J.B., 1988. An internally consistent dataset with uncertainties and
949 correlations: 3. Applications to geobarometry, worked examples and a computer program.
950 Journal of Metamorphic Geology 6, 173–204.
951 Pownall, J.M., 2015. UHT metamorphism on Seram, eastern Indonesia: reaction microstructures and
952 *P–T* evolution of spinel-bearing garnet–sillimanite granulites from the Kobipoto Complex.
953 Journal of Metamorphic Geology 33, 909–935. doi:10.1111/jmg.12153
954 Pownall, J.M., Hall, R., 2014. Neogene extension on Seram: A new tectonic model for the northern
955 Banda Arc. Indonesian Petroleum Association, Proceedings 38, IPA14-G-305.
956 Pownall, J.M., Hall, R., Watkinson, I.M., 2013. Extreme extension across Seram and Ambon, eastern
957 Indonesia: evidence for Banda slab rollback. Solid Earth 4, 277–314. doi:10.5194/se-4-277-
958 2013
959 Pownall, J.M., Hall, R., Armstrong, R.A., Forster, M.A., 2014. Earth's youngest known ultrahigh-
960 temperature granulites discovered on Seram, eastern Indonesia. Geology 42, 279–282.
961 doi:10.1130/G35230.1
962 Pownall, J.M., Hall, R., Lister, G.S., 2016. Rolling open Earth's deepest forearc basin. Geology 44,
963 947–950. doi:10.1130/G38051.1
964 Pownall, J.M., Hall, R., Armstrong, R.A., 2017*a*, Hot lherzolite exhumation, UHT migmatite
965 formation, and acid volcanism driven by Miocene rollback of the Banda Arc, eastern Indonesia.
966 Gondwana Research 51, 92–117. doi:10.1016/j.gr.2017.07.003
967 Pownall, J.M., Forster, M.A., Hall, R., Watkinson, I.M, 2017*b*. Tectonometamorphic evolution of
968 Seram and Ambon, eastern Indonesia: Insights from $^{40}Ar/^{39}Ar$ geochronology. Gondwana
969 Research 44, 35–53. doi:10.1016/j.gr.2016.10.018
970 Priem, H.N.A., Andriessen, P.A.M., Boelrijk, N.A.I.M., Hebeda, E.H., Hutchinson, C.S., Verdurmen,
971 E.A.T., Versschure, R.H., 1978. Isotopic evidence for a middle to late Pliocene age of the

cordierite granite on Ambon, Indonesia. Geologie en Mijnbouw 57, 441–443.
Raimondo, T., Payne, J., Hand, M., Clark, C., Anczkiewicz, R., 2017. Large discrepancies between garnet Lu–Hf and Sm–Nd isochron ages: the problem of inherited Hf. Geophysical Research Abstracts 19, EGU2017-2152.
Roberts, M.P., Finger, F., 1997. Do U–Pb zircon ages from granulites reflect peak metamorphic conditions? Geology 25, 319–322. doi:10.1130/0091-7613(1997)025<0319:DUPZAF>2.3.CO;2
Rubatto, D., 2002. Zircon trace element geochemistry: partitioning with garnet and the link between U-Pb ages and metamorphism. Chemical Geology 184, 123–138. doi:10.1016/S0009-2541(01)00355-2
Rubatto, D., 2017. Zircon: the metamorphic mineral. Reviews in mineralogy and geochemistry 83, 261–295.
Rubatto, D., Hermann, J., 2003. Zircon formation during fluid circulation in eclogites (Monviso, Western Alps): implications for Zr and Hf budget in subduction zones. Geochimica et Cosmochimica Acta 67, 2173–2187. doi:10.1016/S0016-7037(02)01321-2
Rubatto, D., Hermann, J., 2007*a*. Experimental zircon/melt and zircon/garnet trace element partitioning and implications for the geochemistry of crustal rocks. Chemical Geology 241, 38–61.
Rubatto, D., Hermann, J., 2007*b*. Zircon behaviour in deeply subducted rocks. Elements 3, 31–35.
Ryan, W.B.F., Carbotte, S.M., Coplan, J.O., O'Hara, S., Melkonian, A., Arko, R., Weissel, R.A., Ferrini, V., Goodwillie, A., Nitsche, F., Bonczkowski, J., Zemsky, R., 2009. Global multi-resolution topography synthesis. Geochemistry, Geophysics, Geosystems 10.
Sajeev, K., Williams, I.S., Osanai, Y., 2010. Sensitive high-resolution ion microprobe U–Pb dating of prograde and retrograde ultrahigh-temperature metamorphism as exemplified by Sri Lankan granulites. Geology 38, 971–974.
Santosh, M., Wilde, S.A., Li, J.H., 2007. Timing of Paleoproterozoic ultrahigh-temperature metamorphism in the North China Craton: Evidence from SHRIMP U-Pb zircon geochronology. Precambrian Research 159, 178–196.
Sawyer, E.W., 2008. Atlas of Migmatites. The Canadian Mineralogist, Special Publication 9, 371 p.
Schaltegger, U., Fanning, C.M., Günther, D., Maurin, J.C., Schulmann, K., Gebauer, D., 1999. Growth, annealing and recrystallization of zircon and preservation of monazite in high-grade metamorphism: conventional and in-situ U-Pb isotope, cathodoluminescence and microchemical evidence. Contributions to Mineralogy and Petrology 134, 186–201. doi:10.1007/s004100050478
Scherer, E.E., Cameron, K.L., Blichert-Toft, J., 2000. Lu–Hf garnet geochronology: closure temperature relative to the Sm–Nd system and the effects of trace mineral inclusions. Geochimica et Cosmochimica Acta 64, 3413–3432. doi:10.1016/S0016-7037(00)00440-3
Smit, M.A., Scherer, E.E., Mezger, K., 2013. Lu–Hf and Sm–Nd garnet geochronology: Chronometric closure and implications for dating petrological processes. Earth and Planetary Science Letters 381, 222–233.
Spakman, W., Hall, R., 2010. Surface deformation and slab-mantle interaction during Banda arc subduction rollback. Nature Geoscience 3, 562–566. doi:10.1038/ngeo917
Stacey, J.S., Kramers, J.D., 1975. Approximation of terrestrial lead isotope evolution by a two stage model. Earth and Planetary Science Letters 127, 30–45.
Steiger, R.H., Jäger, E., 1977. Subcommission on geochronology: Convention on the use of decay constants in geo- and cosmoschronology. Earth and Planetary Science Letters 36, 359–362.
Taylor, R.J.M., Clark, C., Fitzsimons, I.C.W., Santosh, M., Hand, M., Evans, N., McDonald, B., 2014. Post-peak, fluid-mediated modification of granulite facies zircon and monazite in the Trivandrum Block, southern India. Contributions to Mineralogy and Petrology 168, 1044.

1021 Tedeschi, M., Lanari, P., Rubatto, D., Pedrosa-Soares, A., Hermann, J., Dussin, I., Pinheiro, M.A.P.,
1022 Bouvier, A.-S., and Baumgartner, L., 2017. Reconstruction of multiple P-T-t stages from
1023 retrogressed mafic rocks: Subduction versus collision in the Southern Brasília orogeny (SE
1024 Brazil). Lithos 294–295, 283–303.
1025 Tjokrosapoetro, S., Budhitrisna, T., 1982. Geology and Tectonics of the northern Banda Arc. Bulletin
1026 of the Indonesian Geological Research and Development Centre 6, 1–17.
1027 Tjokrosapoetro, S., Achdan, A., Suwitodirdjo, K., Rusmana, E., Abidin, H. Z., 1993*a*. Geological
1028 map of the Masohi quadrangle, Maluku, 1:250000, Geological Research and Development
1029 Centre, Bandung, Indonesia.
1030 Tjokrosapoetro, S., Rusmana, E., Achdan, A., 1993*b*. Geological map of the Ambon sheet, Maluku,
1031 1:250,000, Geological Research and Development Centre, Bandung, Indonesia.
1032 Tomkins, H.S., Powell, R., and Ellis, D.J., 2007. The pressure dependence of the zirconium-in-rutile
1033 thermometer. Journal of Metamorphic Geology 25, 703–713.
1034 Valk, W., 1945. Contributions to the geology of West Seran, in: Rutten, L., Hotz, W. (Eds.),
1035 Geological, Petrographical, and Palaeontological Results of Explorations, Carried Out From
1036 September 1917 Till June 1919 in the Island of Ceram. De Bussy, Amsterdam, p. 104.
1037 van der Sluis, J.P., 1950. Geology of East Seran, in: Rutten, L., Hotz, W. (Eds.), Geological,
1038 Petrographical, and Palaeontological Results of Explorations, Carried Out From September
1039 1917 Till June 1919 in the Island of Ceram. De Bussy, Amsterdam, p. 67.
1040 Vavra, G., Schmid, R., Gebauer, D., 1999. Internal morphology, habit and U–Th–Pb microanalysis of
1041 amphibolite-to-granulite facies zircons: geochronology of the Ivrea Zone (Southern Alps).
1042 Contrib Mineral Petrol 134, 380–404. doi:10.1007/s004100050492
1043 Watson, E.B., Wark, D.A., Thomas, J.B., 2006. Crystallization thermometers for zircon and rutile.
1044 Contributions to Mineralogy and Petrology 151, 413–433. doi:10.1007/s00410-006-0068-5
1045 Williams, M.L., Jercinovic, M.J., Harlov, D.E., Budzyń, B., Hetherington C.J., 2011. Resetting
1046 monazite ages during fluid-related alteration. Chemical Geology 283(3–4), 218–225.
1047 Yakymchuk, C., and Brown, M., 2014. Behaviour of zircon and monazite during crustal melting.
1048 Journal of the Geological Society 171, 465–479.
1049 Yakymchuk, C., Brown, M., Clark, C., Korhonen, F.J., Piccoli, P.M., Siddoway, C.S., Taylor, R.J.M.,
1050 Vervoort, J.D., 2015. Decoding polyphase migmatites using geochronology and phase
1051 equilibria modelling. Journal of Metamorphic Geology 33, 203–230.
1052 Yakymchuk, C., Clark, C., White, R.W., 2017. Phase relations, reaction sequences and
1053 petrochronology. Reviews in Mineralogy and Geochemistry 83, 13–53.

Figures

Fig. 1. Tectonic map of Eastern Indonesia. The island of Seram is located in the northern limb of the Banda Arc. Tectonic features are from Hall (2012), with the location of the Banda Detachment from Pownall *et al.* (2016). Islands to the north of the Banda Sea once comprised the Sula Spur (Klompé 1954) – a continental promontory extending from NW Australia (Fig. 19d) that fragmented upon collision with western Sulawesi (SE Asia). Base-map elevation data are from Ryan *et al.* (2009). The yellow diamond indicates the sampling locality for the Kobipoto Complex granulites involved in this study. T—Tioor; K—Kur; F—Fadol.

Fig. 2. Geological sketch map of Seram and Ambon, after Valk (1945), Germeraad (1946), van der Sluis (1950), Tjokrosapoetro *et al.* (1993*a*, *b*), Gafoer *et al.* (1993), and Pownall *et al.* (2013, 2014, 2016). Samples KP11-588 and KP11-619 are located in the Kobipoto Mountains. Pen.—Peninsular; Mtns.—Mountains.

Fig. 3. Thin section photomicrographs (PPL) and BSE images of the Kobipoto Complex granulites. Mineral abbreviations are after Kretz (1983). (**a**) Sample KP11-588: Voluminous garnet separated from abundant sillimanite by order reaction microstructures of cordierite + spinel + ilmenite. (**b**) Sample KP11-588: Cordierite corona surrounding garnet, and symplectic spinel and ilmenite adjacent to sillimanite, were produced during retrograde reactions during rapid decompression from peak conditions (see also Pownall 2015). (**c**) Sample KP11-588: Inclusions of spinel + quartz + corundum within garnet – an assemblage indicative of UHT metamorphism. (**d**) Sample KP11-619: Large (4 mm diameter) garnet within leucosome comprising pinitised cordierite (pin), plagioclase, quartz, and biotite. (**e**) Sample KP11-588: BSE image of ordered reaction microstructures between garnet and sillimanite. Cordierite corona features vermicular blobs of quartz adjacent to garnet, and symplectic spinel grains adjacent to sillimanite. Note the zircon inclusion in garnet. (**f**) Sample KP11-619: BSE image of symplectic spinel within cordierite, hosting corundum and tiny blebs of sapphirine (see Pownall 2015).

Fig. 4. Summary of *P–T* data for the Kobipoto Complex granulites and lherzolites, modified after Pownall *et al.* (2017*a*) and Pownall (2015). The purple arrow shows a clockwise *P–T* path for UHT granulite sample KP11-588, passing though peak conditions of 925 ± 50˚C at 9 ± 1 kbar. Reaction lines for garnet (Grt), cordierite (Crd), biotite (Bt), and silicate melt (Liq) are taken from a *P–T* pseudosection calculated specifically for the melanosome using THERMOCALC in the Na_2O–CaO–K_2O–FeO–MgO–Al_2O_3–SiO_2–H_2O–TiO_2–Fe_2O_3 (NCKFMASHTO) chemical system. Post-peak equilibration conditions of 754 ± 116˚C and 4 ± 1 kbar are based on a THERMOCALC 'Ave*PT*' calculation for the cordierite- and spinel-dominated reaction microstructures, using the garnet rim composition (Pownall 2015). The blue arrow shows the *P–T* evolution of the adjacent lherzolites, which juxtaposed against the granulites provided the heat for UHT metamorphism (Pownall *et al.* 2017*a*).

Fig. 5. Summary of U–Pb zircon ages obtained for the Kobipoto Complex granulites (after Pownall *et al.* 2017*a*). Note the cluster of R_m zircon ages at *c*. 16 Ma, the occurrence of some R_m ages at *c*. 23 Ma (correlating with the initial collision of Australia with SE Asia; Hall 2011), and the broad spread of R_2 zircon ages between 215 and 173 Ma. We do not imply that R_m zircon rim populations at *c*. 16 Ma and 23–19 Ma were formed by the same process, only that they have identical textural relationships. The 'cartoon' zircon is lifted from Fig. 8b.

Fig. 6. Textural settings of zircon, monazite, and rutile in granulite KP11-588. Mineral abbreviations are after Kretz (1983). (**a**) Zircon inclusion within garnet that also contains small melt inclusions (MI) and a biotite inclusion (PPL image). See Fig. 9b for CL image of this grain. (**b**) Zircon grains present within cordierite corona and included within garnet (XPL image). (**c**, **d**) Monazite grains dated *in situ* as part of this study. The ablation pit numbers correspond to those in Table 2 and Fig. 10. (**e**, **f**) Rutile grains analysed *in situ* for Zr-in-rutile thermometry. Analytical spots correspond to those in Table 4. Rutile grains in the leucosome record UHT conditions (> 900˚C), whereas those included in garnet have significantly lower Zr concentrations that yield lower temperatures (~600–750˚C).

Fig. 7. Melt inclusions (MI) within garnet of sample KP11-588 (photomicrographs, PPL). Note the occurrence of both primary inclusions (square in thin section), and secondary melt inclusions located along planar defects, as shown by the red arrow in part (**a**).

Fig. 8. (**a**) CL images of zircons from sample KP11-588 analysed as part of this study. Note the distinctive cores (C_d), 1st overgrowth zones (R_2), and CL-dark rims (R_m). Ages follow Pownall *et al.* (2017*a*). (**b**) Cartoons of selected zircon grains demonstrating the relationships between the different generations of growth (after Pownall *et al.* 2017*a*). Note also the occurrence of very thin (too thin to analyse) outermost 'R_0' zircon rims on some grains.

Fig. 9. CL images of zircons acquired *in situ* from a thin section of sample KP11-588. (**a**) Zircons located in the post-peak reaction microstructures at the boundary with leucosome and included with a large lath of sillimanite feature thick R_m rims (dark in CL) overgrowing R_2 zones (bright in CL) and detrital cores (C_d). The CL images annotate a XPL thin section photo of the same zircon grains, showing their textural locations. (**b**–**e**) Zircons included within garnet do not feature R_m rims, just CL-bright R_2 zones around detrital cores (C_d). In part (**b**), the CL image annotates a PPL thin section photo of the same zircon grain, located > 200 μm from the rim of the garnet it is included in. Mineral abbreviations are after Kretz (1983).

Fig. 10. Tera-Wasserburg plot for SHRIMP U–Pb analysis of monazite from sample KP11-588. The mean $^{206}Pb/^{238}U$ age is quoted to 95% confidence, and error ellipses are drawn at 68.3% confidence. An upper intercept (common Pb $^{207}Pb/^{206}Pb$) value of 0.837 is based on the model of Stacey & Kramers (1975). MSWD—mean square of weighted deviates. See Table 2 for U–Pb geochronology data.

Fig. 11. (**a**) Major element zonation profile through representative garnet in sample KP11-588 determined from electron microprobe line-scan (modified after Pownall 2015). Garnet composition is expressed in terms of the following end-members: almandine (alm) = $Fe^{2+}/(Fe^{2+} + Mn + Mg + Ca)$; pyrope (pyr) = $Mg/(Fe^{2+} + Mn + Mg + Ca)$; spessartine (sps) = $Mn/(Fe^{2+} + Mn + Mg + Ca)$; grossular (grs) = $Ca/(Fe^{2+} + Mn + Mg + Ca)$. The location of this line-scan in show in part (**b**) – a backscattered electron image coloured according to backscatter intensity that displays the geometry of the major element garnet zonation profile. Major element concentrations are flat in the central region, displaying evidence for resorption close to the rim (with increase in spessartine component). Unlike as depicted by HREE zoning (Fig. 12), there is no evidence for a separate core region.

Fig. 12. HREE abundances (linear scale) and concentrations of Lu, Sm, Nd, and Hf (log scale) obtained along a 1.1 mm LA-ICP-MS laser traverse through garnet from KP11-588 (ablation track through garnet shown at bottom). The HREE profiles demonstrate the occurrence of a distinct core region (shaded grey), but it was unfortunately not possible to manually separate garnet cores and

rims for the Lu–Hf and Sm–Nd dating. Three additional laser transects (not shown) were performed, with similar results. See the Supplementary Files for the full dataset.

Fig. 13. REE plot comparing R_m zircon, R_2 zircon, and garnet. Zircon from samples KP11-588 and KP11-619 was analysed by SHRIMP II at Geoscience Australia, and the garnet data were acquired by LA-ICP-MS laser transects (Fig. 12), as described in the text. The concentrations are normalised to CI chondrite values (McDonough & Sun 1995). The broad spread in garnet HREE concentrations is due to the differences in abundance between the core (relatively enriched) and rim (relatively depleted), as labelled (and evident in Fig. 12). This plot shows that HREE abundances of *c*. 16 Ma R_m zircon are within the range of garnet HREE abundances, but the *c*. 200 Ma R_2 zircon concentrations are an order of magnitude higher. See the Supplementary Material for full datasets.

Fig. 14. Th versus U plots of zircon from samples KP11-588, KP11-691, and KP11-621 analysed by SHRIMP (Pownall *et al.* 2017*a*). KP11-621 is a Kobipoto Complex cordierite diatexite also from the Kobipoto Mountains (see Table 1). Grey dashed lines contour fixed Th/U ratios. Analyses are coloured according to the type of zircon analysed: black circles for detrital cores (C_d); white circles for metamorphic overgrowths (R_m); and diamonds for CL-bright 'R_2' zones.

Fig. 15. Results of Ti-in-zircon thermometry acquired for zircon from samples KP11-588 and KP11-619. The shaded regions are drawn for the Ferry & Watson (2007) calibration, and demonstrate a notable difference in temperature between R_m zircon (~600˚C) and R_2 zircon (~700˚C). The activities of SiO_2 and TiO_2 were assumed here to both equal 1 for application of the Ferry & Watson (2007) thermometer (although lowering $a SiO_2$ by 0.1 lowers temperatures by ~15˚C). See Table 3 for Ti concentrations and full thermometry results.

Fig. 16. Results of Zr-in-rutile thermometry (of Tomkins *et al.* 2007) calculated for rutile from sample KP11-588. Pressure was set at 9 kbar in order to correspond to the peak metamorphic *P–T* conditions calculated by Pownall (2015). The Ferry & Watson (2007) Zr-in-rutile thermometers (assuming $a SiO_2 = 1$) gave extremely similar results (Table 4), which for clarity have not been plotted. The overlaid histogram (red bars) is binned at 50˚C intervals. The three rutile grains analysed from the leucosome (Fig. 6f) yielded the hotter temperatures than those included in garnet (Fig. 6e).

Fig. 17. Lu–Hf and Sm–Nd garnet geochronology of sample KP11-588. (**a**) Lu–Hf isochron diagram. Error bars are smaller than the symbols. w.r.—whole rock. See Table 5 for results. (**b**) Sm–Nd isochron diagram. w.r.—whole rock. The grt-2 fraction, $^{143}Nd/^{144}Nd$ analysed to higher precision by IsotopX Pheonix ID-TIMS (grt 2*), is plotted in green. See Table 6 for results. (**c**) Garnet Lu–Hf mixing model for KP11-588. Combining 80% 16 Ma garnet rims (1 ppm Lu; 0.03–0.07 ppm Hf) with 20% 200 Ma garnet cores (25 ppm Lu; 0.34 ppm Hf) produces a mixed model age between 116.5 and 151.2 Ma (green region), which is consistent with the measured Lu–Hf age of 138.6 ± 0.7 Ma. For clarity, only the grt-1 2-point isochron is shown.

Fig. 18. Compilation of geochronology results for the Kobipoto Complex UHT granulites. U–Pb zircon ages are from Pownall *et al.* (2017*a*), and the $^{40}Ar/^{39}Ar$ biotite age is from Pownall *et al.* (2017*b*). All results are obtained for sample KP11-588, except the $^{40}Ar/^{39}Ar$ age that was obtained for KP11-619, and the age range of the R_2 zircon U–Pb dates, which are a combination of all Kobipoto Complex migmatite samples presented by Pownall *et al.* (2017*a*).

Fig. 19. Explanation of zircon, garnet, monazite, and rutile histories for the Kobipoto Complex granulites linked to tectonic reconstruction of the Banda region (Hall 2012). The reconstructions (for

80–130˚E, 0–50˚S) show oceanic crust in mint green (older than 120 Ma) and mid-blue (younger than 120 Ma), and submarine arcs and oceanic plateaus in pale blue. The yellow diamond indicates the location of central Seram. *P–T* values (orange boxes) are from Pownall (2015) and Ti-in-zircon thermometry (Fig. 15). The cartoon minerals are not to scale. (**a**) Australian detrital zircon (C_d) was deposited as part of the Kobipoto Complex protolith in the Late Triassic. (**b**) Upper amphibolite-facies metamorphic event(s) between 216 and 170 Ma grew R_2 zircon and garnet cores. (**c**) No known event occurred at 138 Ma. (**d**) UHT metamorphism affected the Kobipoto Complex just prior to 16 Ma. Prograde peritectic growth of garnet rims trapped melt. Major element and LREE cations equilibrated between core and rim, but more retentive HREEs were largely retained in the core. Rutiles in the leucosome recorded >900˚C Zr-in-Rt temperatures. (**e**) Upon rapid decompression and cooling from UHT conditions, consumption of garnet liberated Zr and LREEs that facilitated the growth of *c*. 16 Ma R_m zircon and monazite, respectively. Zircon shielded in garnet did not record the UHT event. 138 Ma garnet Lu–Hf age is the result of mixing between cores and rims. Sketch cross-section adapted from Pownall (2015).

Tables

Table 1

Table 1. *Previous geochronology of the Kobipoto Complex migmatites, eastern Indonesia*

Author(s)	Sample	Rock	Location			Age (Ma)			
				Long. (˚E)	Lat. (˚S)	Rb–Sr	K–Ar	$^{40}Ar/^{39}Ar$	SHRIMP U–Pb zircon
Priem *et al.* (1978)		Crd diatexite	Ambon			3.3 ± 0.1†	3.8 ± 0.2‡		
Honthaas *et al.* (1997)	Kur7H	Granodiorite	Kur	131.99*	5.35*			17.07 ± 0.40‡ 23.05 ± 0.55§	
	Kur7G	Diorite	Kur	131.99*	5.35*			18.94 ± 0.51†	
	Kur7J	Paragneiss	Kur	131.99*	5.35*			16.93 ± 0.39‡ 17.64 ± 0.41§	
Honthaas *et al.* (1999)	(several)	Crd diatexite	Ambon				4.22–3.29‡ 4.75–3.99†		
Linthout *et al.* (1996)	BK18	Crd diatexite	Kaibobo Peninsula	128.17*	3.19*			5.51 ± 0.02‡	
J. Decker (pers. comm. 2011)	10DJ307	Diatexite	Latimor (Ambon)	128.2168	3.7178				3.5 ± 0.1
	10JD306	Diatexite	Latimor (Ambon)	128.2440	3.7370				3.6 ± 0.1
	10JD308	Diatexite	Latimor (Ambon)	128.1302	3.7450				3.3 ± 0.1
	10JD465	Diatexite	Hitu (Ambon)	128.0229	3.7550				3.1 ± 0.1
Pownall *et al.* (2017*a*) **	KP11-588	Grt-Sil granulite	Kobipoto Mountains	129.4786	3.0019				15.8 ± 0.3
	KP11-619	Grt-Crd-Sil metatexite	Kobipoto Mountains	129.4735	3.0168			16.34 ± 0.04‡	16.0 ± 0.6
	KP11-621	Crd diatexite	Kobipoto Mountains	129.4785	3.0022				16.2 ± 0.3
	SE10-178	Diatexite	Kaibobo Peninsula	128.1736	3.1884				6.0 ± 0.2
	KB11-336	Diatexite	Kaibobo Peninsula	128.1787	3.2005				5.5 ± 0.2
	AB11-026	Leucogranite	Latimor (Ambon)	128.2210	3.7192				3.5 ± 0.1
Pownall *et al.* (2017*b*)	SE10-178	Diatexite	Kaibobo Peninsula	128.1736	3.1884			5.88 ± 0.05‡ 6.69 ± 0.13‡	
	KB11-367	Mylonitised crd diatexite	Kaibobo Peninsula	128.2024	3.2173			5.40 ± 0.21‡ 3.30 ± 0.04‡	
	AM10-167	Crd diatexite	S Latimor, Ambon	128.2447	3.7379			3.63 ± 0.04‡	
	KP11-593	Phlogopite lamprophyre	Kobipoto Mountains	129.4802	3.0006			15.07 ± 0.08¶	

*locations estimated from maps in Figure 1c of Honthaas *et al.* (1997) and Figure 2 of Linthout *et al.* (1996), respectively.
†age obtained from a whole rock powder
‡age obtained for biotite (pairs of ages sometimes interpreted for the same sample relate to different Ar reservoirs; see Pownall *et al.* 2017*b*)
§age obtained for K-feldspar
¶age obtained for phlogopite from a lamprophyric dyke intruded through Kobipoto Complex lherzolites
**ages for KP11-588, KP11-619, and KP11-621 reported initially by Pownall *et al.* (2014)

Table 2

Table 2. *U–Pb monazite geochronology, sample KP11-588*

Analytical Spot	% $^{206}Pb_c$	U (ppm)	$^{206*}Pb$ (ppm)	$^{232}Th/^{238}U$	$^{206}Pb/^{238}U$ Age†		Total $^{238}U/^{206}Pb$		Total $^{207}Pb/^{206}Pb$		$^{206}Pb^*/^{238}U$†	
					Ma	± 1 σ		± 1 σ		± 1 σ		± (%)
2.1‡	7.72	2494	32922	14	16.7	0.4	356	2.4	0.1074	1.4	0.002590	0.78
1.1§	12.80	541	51957	99	15.3	0.9	368	5.9	0.1475	2.8	0.002370	1.89
1.2§	8.72	457	54796	124	16.3	0.6	361	3.6	0.1153	5.3	0.002530	1.18
1.3§	9.45	793	86551	113	16.4	0.3	356	1.5	0.1211	3.2	0.002547	0.50

Pb_c and Pb^* indicate the common and radiogenic portions, respectively.
†Common Pb corrected by assuming $^{206}Pb/^{238}U$–$^{207}Pb/^{235}U$ age-concordance
‡Intra-garnet monazite
§Matrix monazite

Table 3

Table 3. *Ti-in-zircon thermometry*

Analytical Spot	Zircon type	Ti (ppm)	±	Watson *et al.* (2006) thermometer			Ferry & Watson (2007) thermometer*		
				T (°C)	+	–	*T* (°C)	+	–
KP11-619-16.1	R_m	1.01	0.05	573	164	12	568	29	22
KP11-619-10.1	R_m	1.05	0.08	575	165	14	570	31	21
KP11-619-18.1	R_m	1.06	0.06	576	165	13	571	30	22
KP11-588-13.1	R_m	1.56	0.06	600	168	12	597	30	24
KP11-619-11.1	R_m	1.68	0.03	605	167	11	602	29	26
KP11-588-24.1	R_2	5.54	0.24	692	187	15	693	36	27
KP11-588-5.3	R_2	5.67	0.16	693	186	13	695	34	29
KP11-588-6.2	R_2	6.88	0.12	709	188	13	712	34	30

Results of Ti-in-zircon thermometry applied to R_m and R_2 zircon from sample KP11-619 and KP11-588. Ti concentrations were measured using SHRIMP II at Geoscience Australia. See Fig. 15 for a graphical representation of these data.
*assuming that $a SiO_2 = a TiO_2 = 1$

Table 4

Table 3. *Zr-in-rutile thermometry*

Analytical Spot	rutile location	Zr (ppm)	±	Ferry & Watson (2007) thermometer*			Tomkins *et al.* (2007) thermometer†		
				T (˚C)	+	–	*T* (˚C)	+	–
rt1	in leucosome‡	3816	365	907	12	13	907	12	13
rt7	in leucosome	3269	365	887	14	15	887	14	15
rt6	in leucosome	3138	333	882	13	14	882	13	14
rt28	in Grt	1569	118	799	8	9	800	8	8
rt29	in Grt	1053	140	757	13	14	758	13	14
rt17	in Grt; adj. Ilm	852	90	736	10	11	737	10	11
rt27	in Grt	806	82	731	9	10	732	9	10
rt14	in Grt; adj. Ilm	614	47	705	7	7	706	7	7
rt11	in Grt; adj. Ilm	601	51	703	7	8	705	7	8
rt13	in Grt; adj. Ilm	583	60	700	9	10	702	9	10
rt15	in Grt	544	46	694	7	8	696	7	8
rt12	in Grt; adj. Ilm	513	77	689	13	14	690	13	14
rt4	in Grt	451	161	678	27	37	679	27	37
rt16	in Grt	413	33	670	7	7	672	7	7
rt5	in Grt	302	45	644	11	13	646	11	13
rt33	in Grt; adj. Ilm	270	33	635	9	10	637	9	10
rt24	in Grt; adj. Ilm	256	23	631	7	7	633	7	7
rt25	in Grt; adj. Ilm	201	13	612	5	5	614	5	5
rt3	in Grt	154	17	593	8	8	595	8	8
rt2	in Grt	149	30	591	13	16	593	13	16

Results of Zr-in-rutile thermometry for sample KP11-588 only. Zr concentrations were measured by LA-ICP-MS at the RSES, ANU. Uncertainties are given to 2SE. adj.—adjacent to. See Fig. 16 for a graphical representation of these data.
*assuming that $a SiO_2 = 1$
†for $P = 9$ kbar
‡at the leucosome margin, also in direct contact with garnet (see Fig. 6f)

Table 5

Table 5. *Lu–Hf geochronology results, sample KP11-588*

	Lu (ppm)	Hf (ppm)	$^{176}Lu/^{177}Hf$ ± 2SE	$^{176}Hf/^{177}Hf$ ± 2SE	Lu–Hf age (Ma) ± 2σ
grt-1	5.205	0.341	2.16141 ± 0.00648	0.28806 ± 0.00003	138.6 ± 0.7
grt-2	5.177	0.334	2.19218 ± 0.00658	0.28811 ± 0.00002	137.9 ± 0.6
w.r.	1.11	0.951	0.16500 ± 0.00050	0.28289 ± 0.00001	

Lu and Hf abundances determined by IsoProbe MC-ICP-MS
w.r.—whole rock; SE—standard error; σ—standard deviation

Table 6

Table 6. *Sm–Nd geochronology results, sample KP11-588*

	Sm (ppm)	Nd (ppm)	$^{147}Sm/^{144}Nd \pm 2SE$	$^{143}Nd/^{144}Nd \pm 2SE$	Sm–Nd age (Ma) ± 2σ
grt-1	7	17	0.21205 ± 0.00021	0.51206 ± 7E–6	6.0 ± 14.0
grt-2	7	17	0.25563 ± 0.00026	0.51206 ± 7E–6	7.1 ± 9.8
grt-2*				0.512067 ± 4E–6	10.6 ± 7.7
w.r.	7.8	39.5	0.11002 ± 0.00011	0.51206 ± 6E–6	

*$^{143}Nd/^{144}Nd$ determined to higher precision by IsotopX Pheonix TIMS. The other data are from IsoProbe MC-ICP-MS.
w.r.—whole rock; SE—standard error; σ—standard deviation.

Figure 1

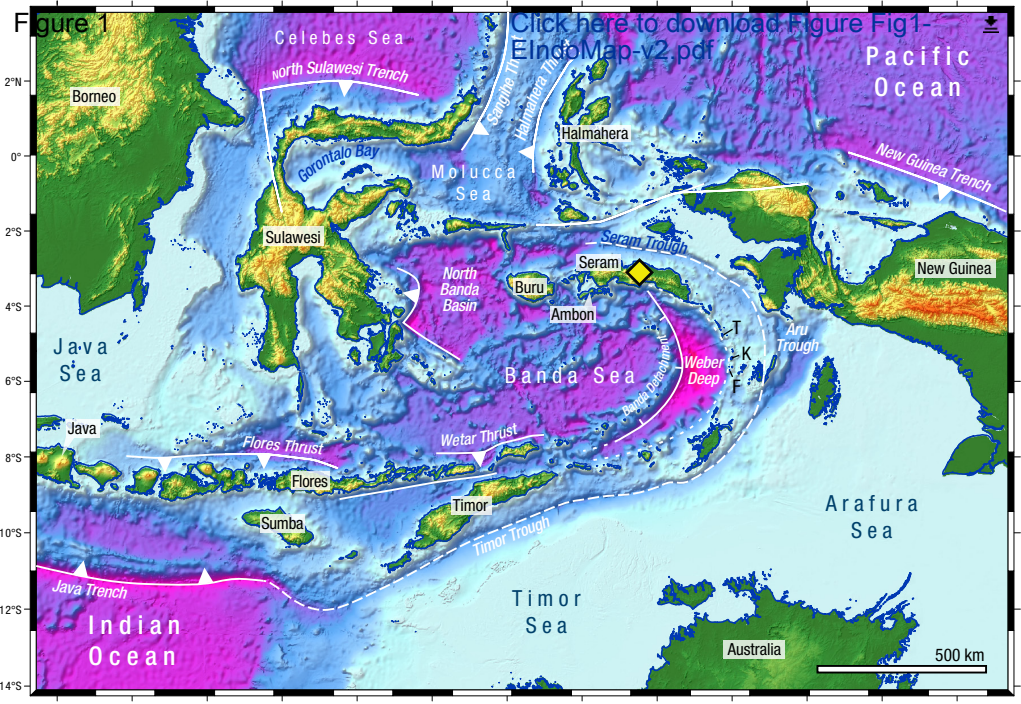
Click here to download Figure Fig1-EIndoMap-v2.pdf
Celebes Sea
North Sulawesi Trench
Sangihe Trench
Halmahera Trench
Pacific Ocean
Borneo
Halmahera
Gorontalo Bay
Molucca Sea
New Guinea Trench
Sulawesi
Seram Trough
Seram
New Guinea
North Banda Basin
Buru
Ambon
Java Sea
T
K
F
Aru Trough
Banda Sea
Weber Deep
Banda Detachment
Java
Flores Thrust
Wetar Thrust
Flores
Timor
Sumba
Arafura Sea
Timor Trough
Java Trench
Indian Ocean
Timor Sea
Australia
500 km
2°N
0°
2°S
4°S
6°S
8°S
10°S
12°S
14°S
114°E
116°E
118°E
120°E
122°E
124°E
126°E
128°E
130°E
132°E
134°E
136°E
138°E
trench / thrust
trough
fault
Banda Detachment
eastern extent of Banda Detachment

Figure 2

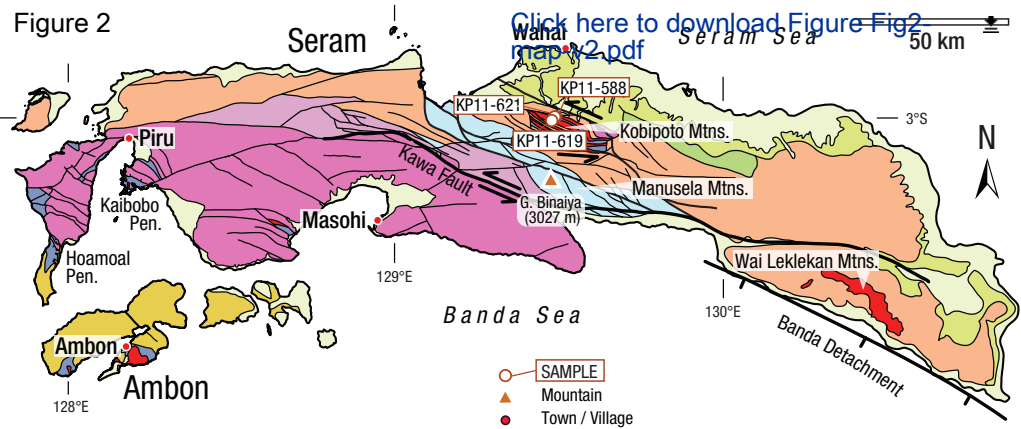
Click here to download Figure Fig2-map 3-2.pdf
Seram
Wahai
Seram Sea
50 km
KP11-588
KP11-621
KP11-619
Kobipoto Mtns.
3°S
N
Piru
Kawa Fault
Kaibobo Pen.
Masohi
G. Binaiya (3027 m)
Manusela Mtns.
Hoamoal Pen.
129°E
Wai Leklekan Mtns.
130°E
Banda Sea
Banda Detachment
Ambon
Ambon
128°E
SAMPLE
Mountain
Town / Village
Fufa & Wahai Beds
Mud- and siltstones
Salas Block Clay
?Olistostrome
Manusela Mtns Limestone
Carbonates & shales
Kanikeh Fm
Clays & siltstones
Saku Fm
Tehoru Fm & Taunusa Cmplx
Slate & marble and amphibolites
Micaschists
Kobipoto Complex
Granulite-facies migmatites (inc. UHT)
Peridotite
Volcanic rocks
Alluvium

Figure 3

Click here to download Figure Fig3-Photos-opti.pdf

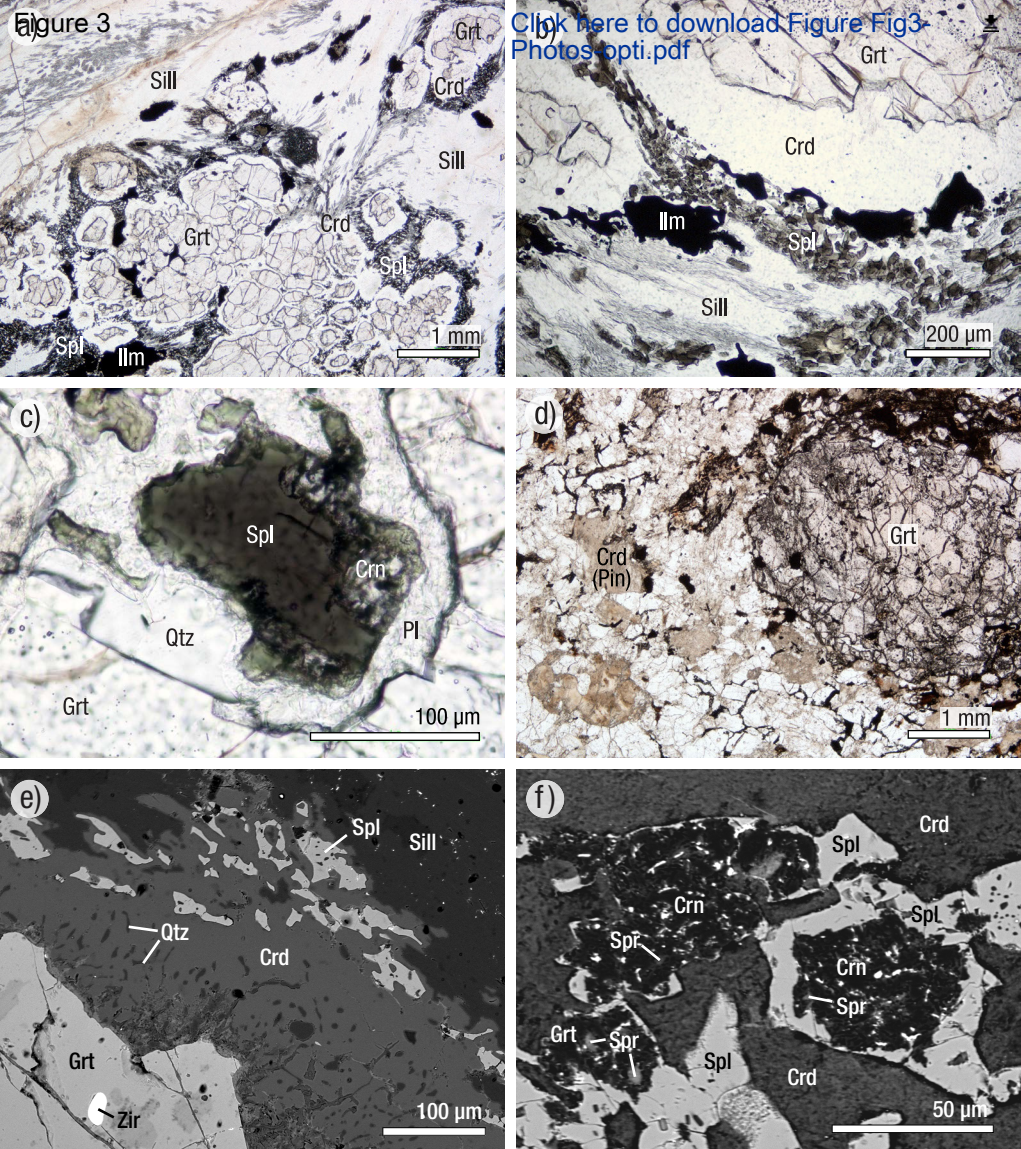

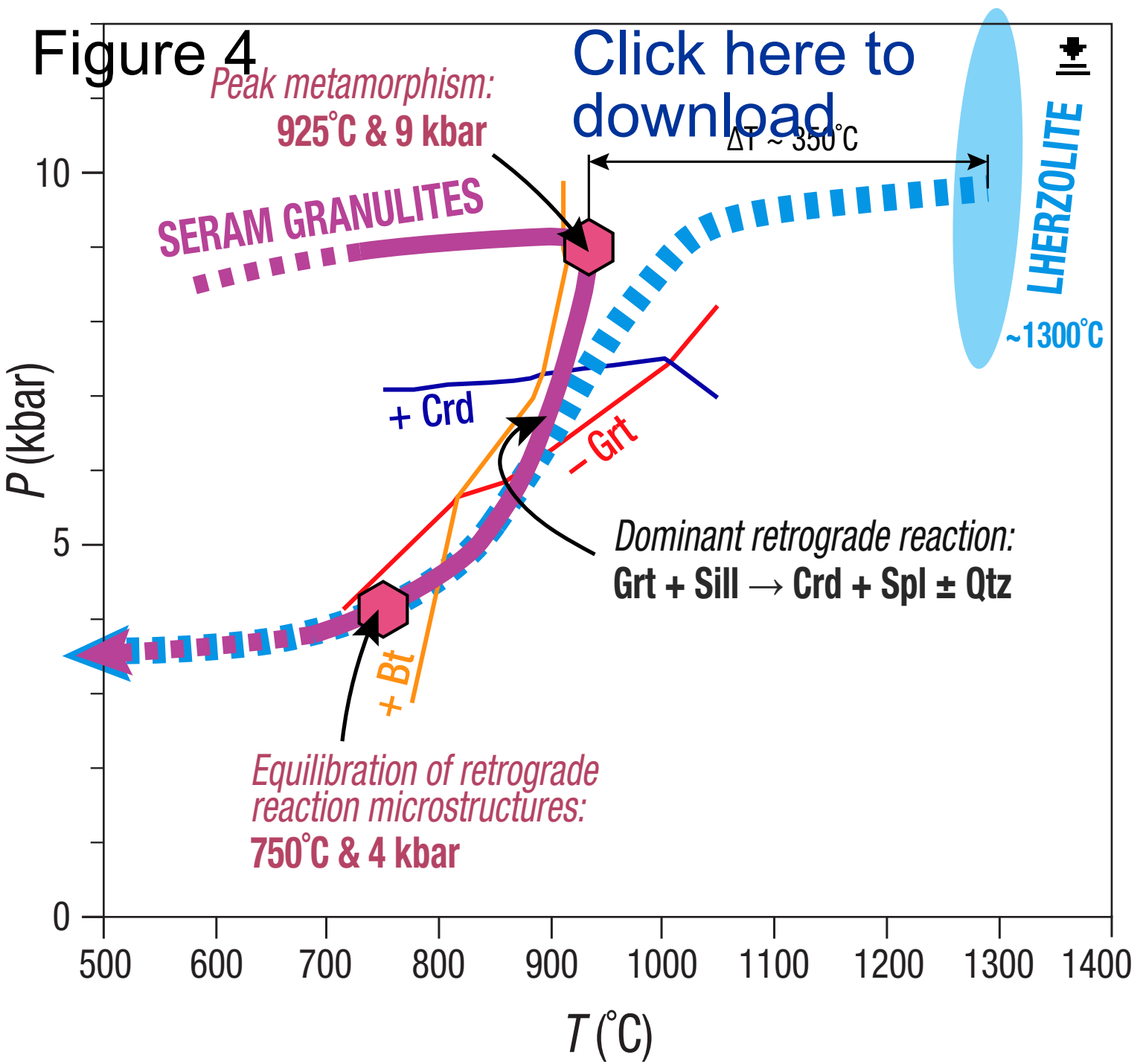
Figure 4
Click here to download
Peak metamorphism:
925°C & 9 kbar
SERAM GRANULITES
ΔT ~ 350°C
LHERZOLITE
~1300°C
+ Crd
– Grt
+ Bt
Dominant retrograde reaction:
Grt + Sill → Crd + Spl ± Qtz
Equilibration of retrograde reaction microstructures:
750°C & 4 kbar
P (kbar)
T (°C)
0
5
10
500
600
700
800
900
1000
1100
1200
1300
1400

Figure 5

Click here to download

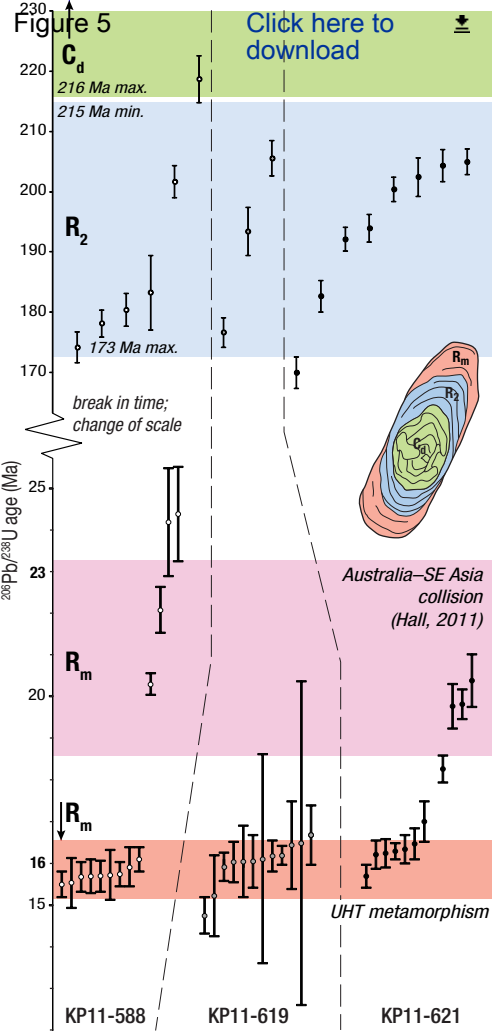

Figure 6

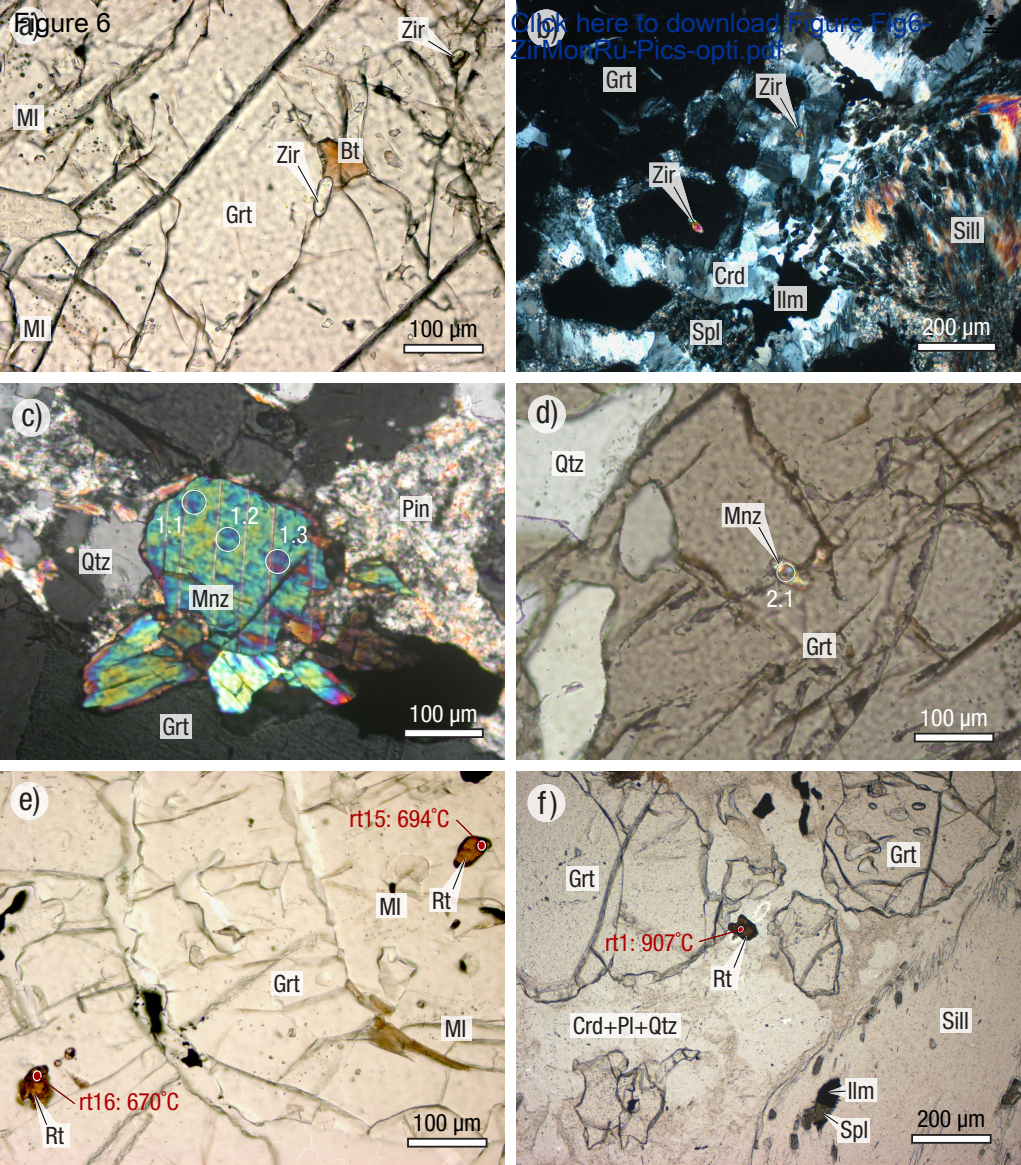

Figure 7

Click here to download

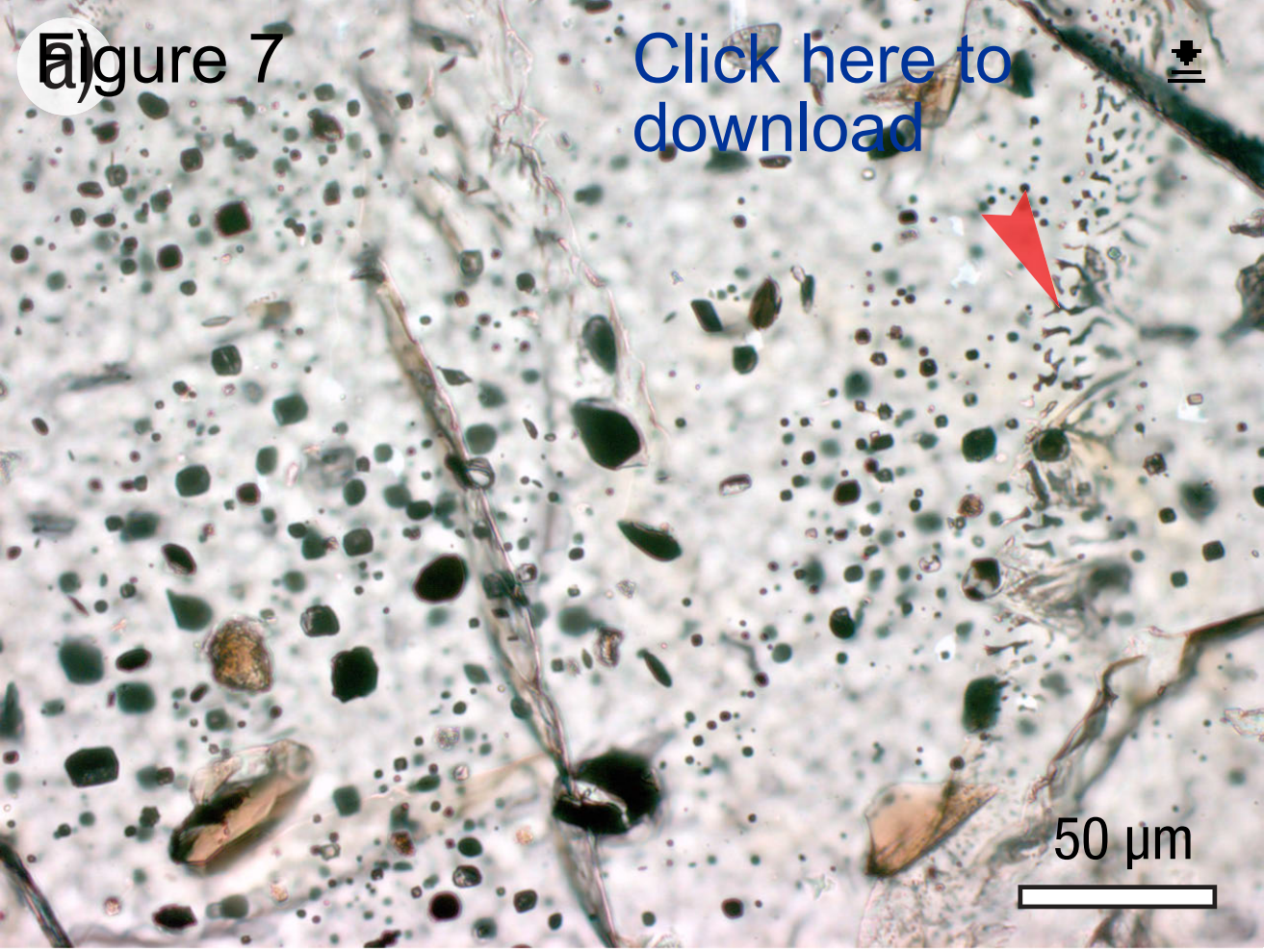

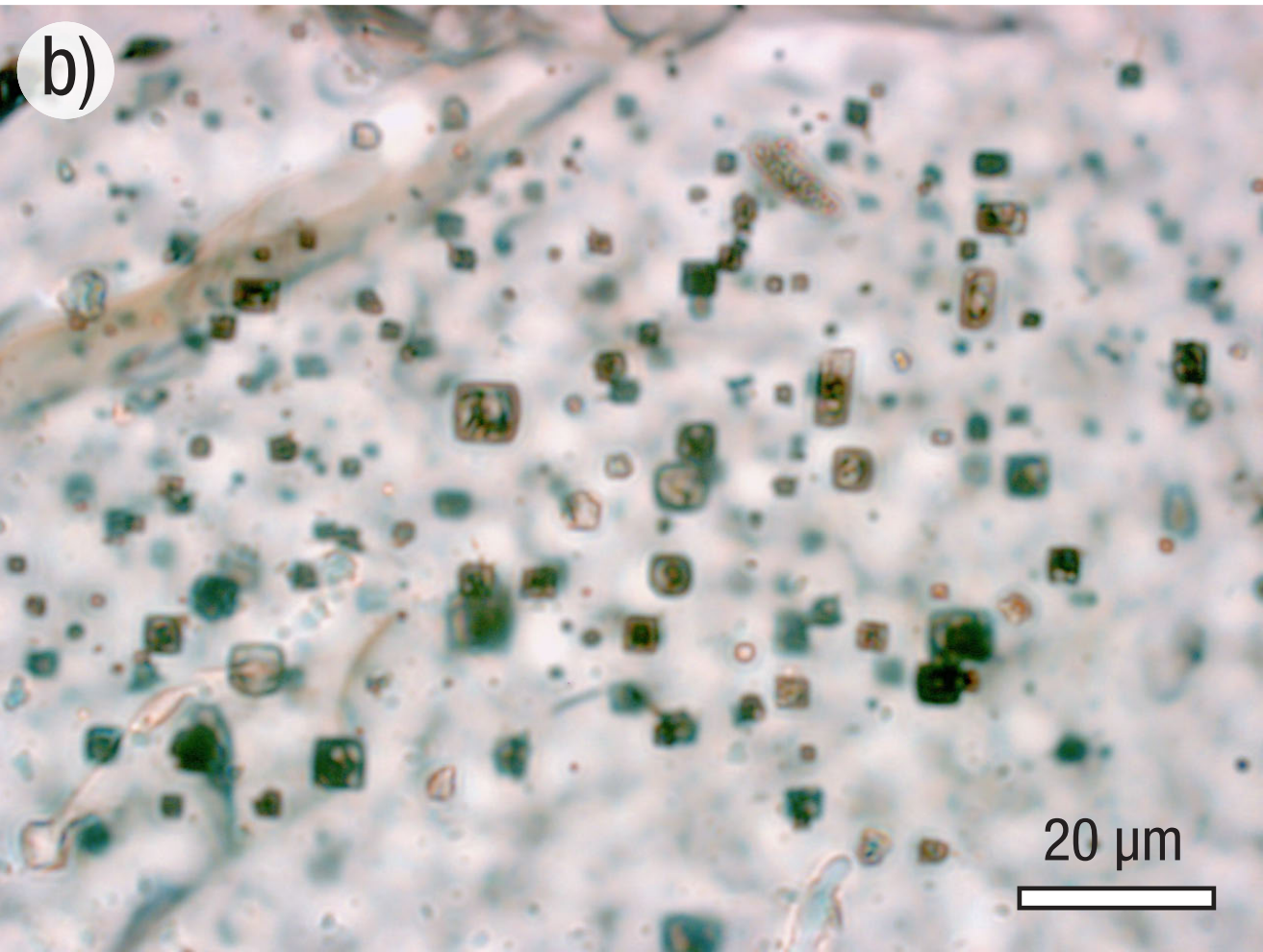

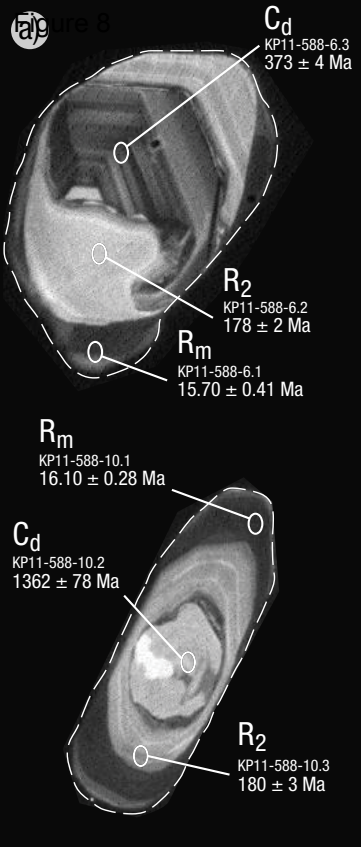

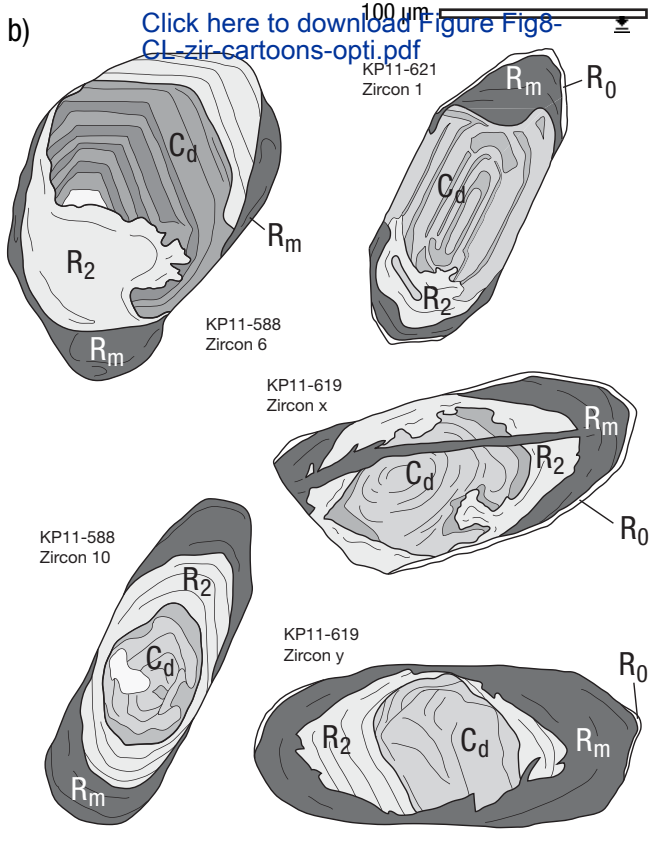

Figure 9

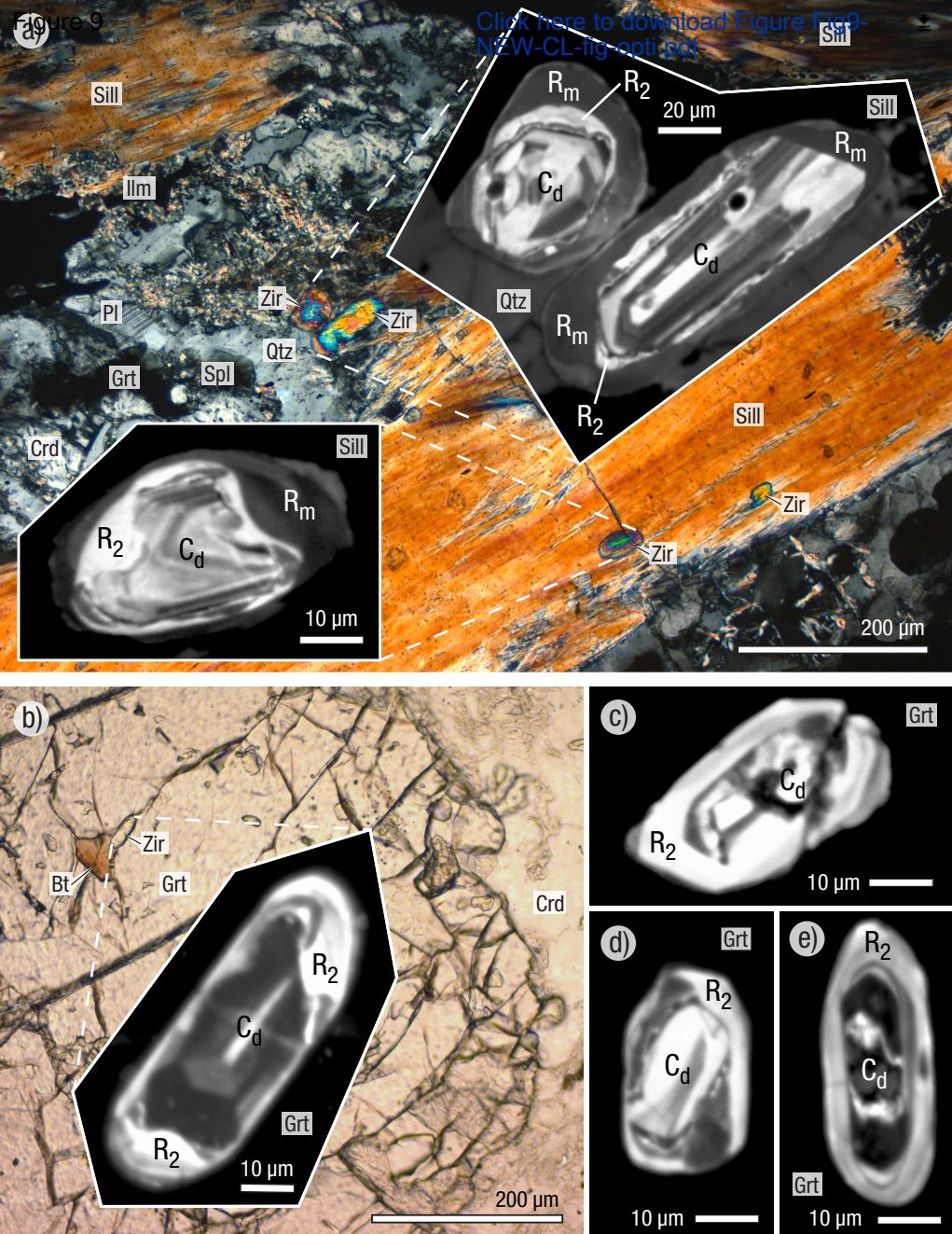

Figure 10

Click here to download

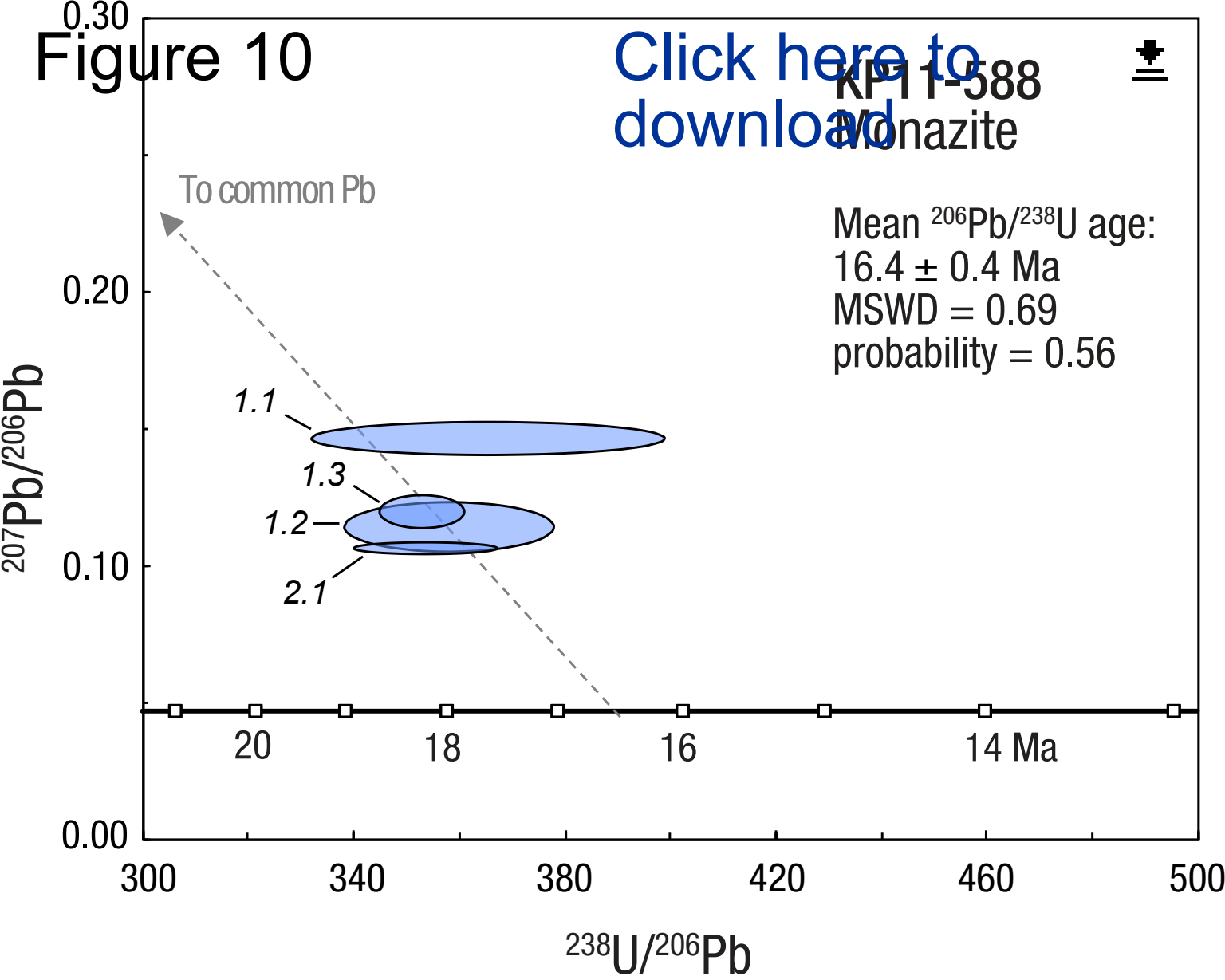

Figure 11

Click here to download

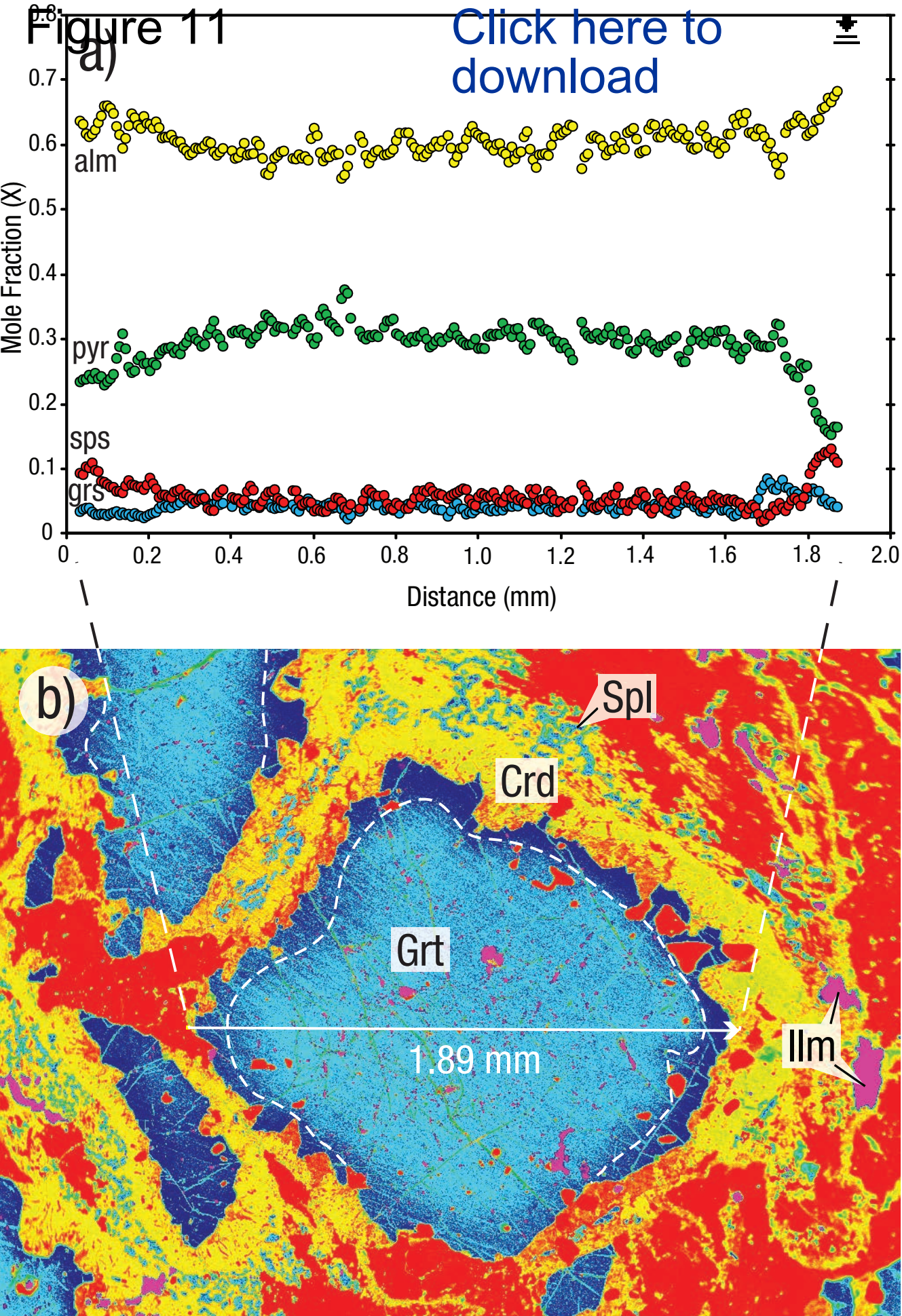

Figure 12

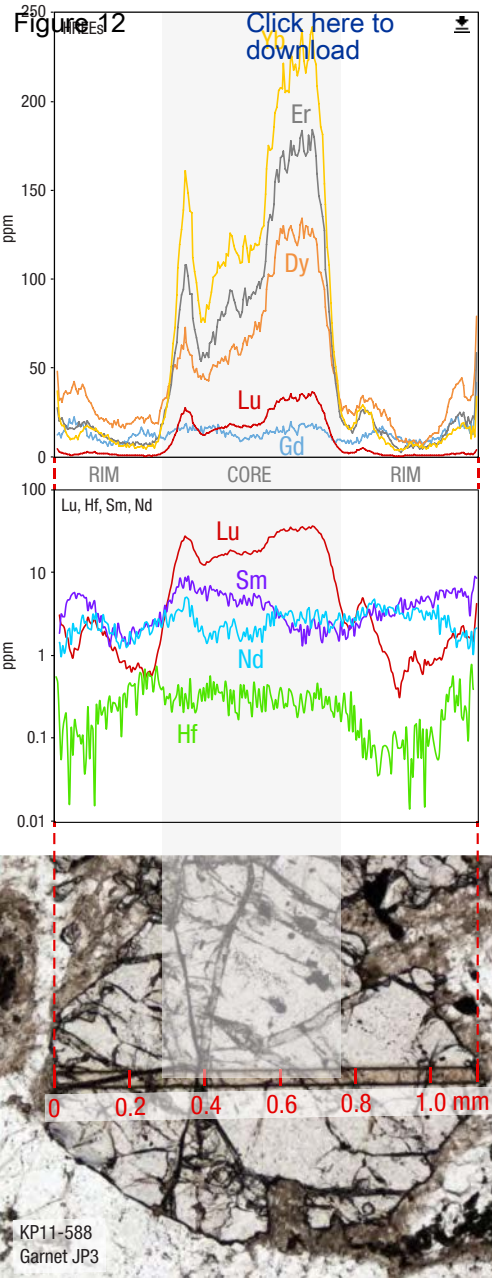
Click here to download
HREEs
Yb
Er
Dy
Lu
Gd
ppm
250
200
150
100
50
0
RIM
CORE
RIM
Lu, Hf, Sm, Nd
Lu
Sm
Nd
Hf
100
10
1
0.1
0.01
0
0.2
0.4
0.6
0.8
1.0 mm
KP11-588
Garnet JP3

Figure 13

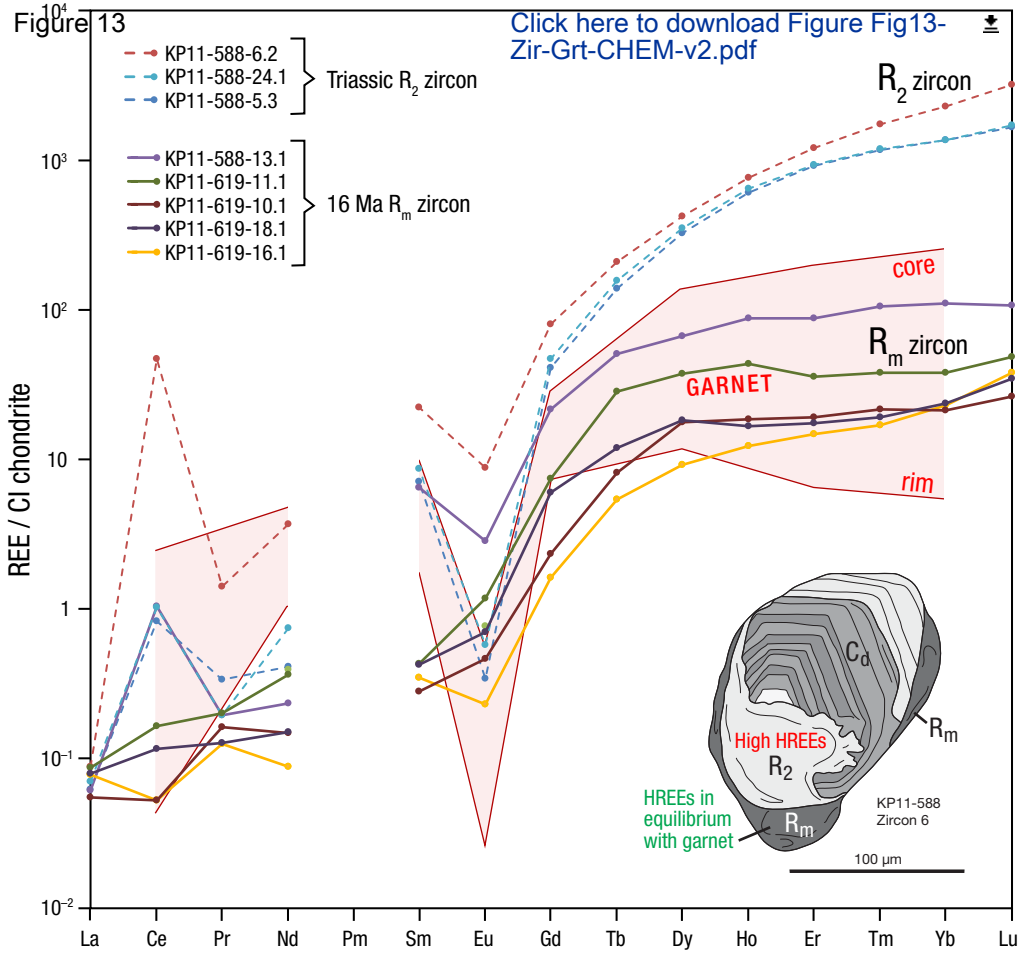
Click here to download Figure Fig13-Zir-Grt-CHEM-v2.pdf
KP11-588-6.2
KP11-588-24.1
KP11-588-5.3
Triassic R2 zircon
KP11-588-13.1
KP11-619-11.1
KP11-619-10.1
KP11-619-18.1
KP11-619-16.1
16 Ma Rm zircon
R2 zircon
core
Rm zircon
GARNET
rim
REE / CI chondrite
10⁴
10³
10²
10
1
10⁻¹
10⁻²
La
Ce
Pr
Nd
Pm
Sm
Eu
Gd
Tb
Dy
Ho
Er
Tm
Yb
Lu
Co
Rm
High HREEs
R2
HREEs in equilibrium with garnet
Rm
KP11-588 Zircon 6
100 µm

Figure 14

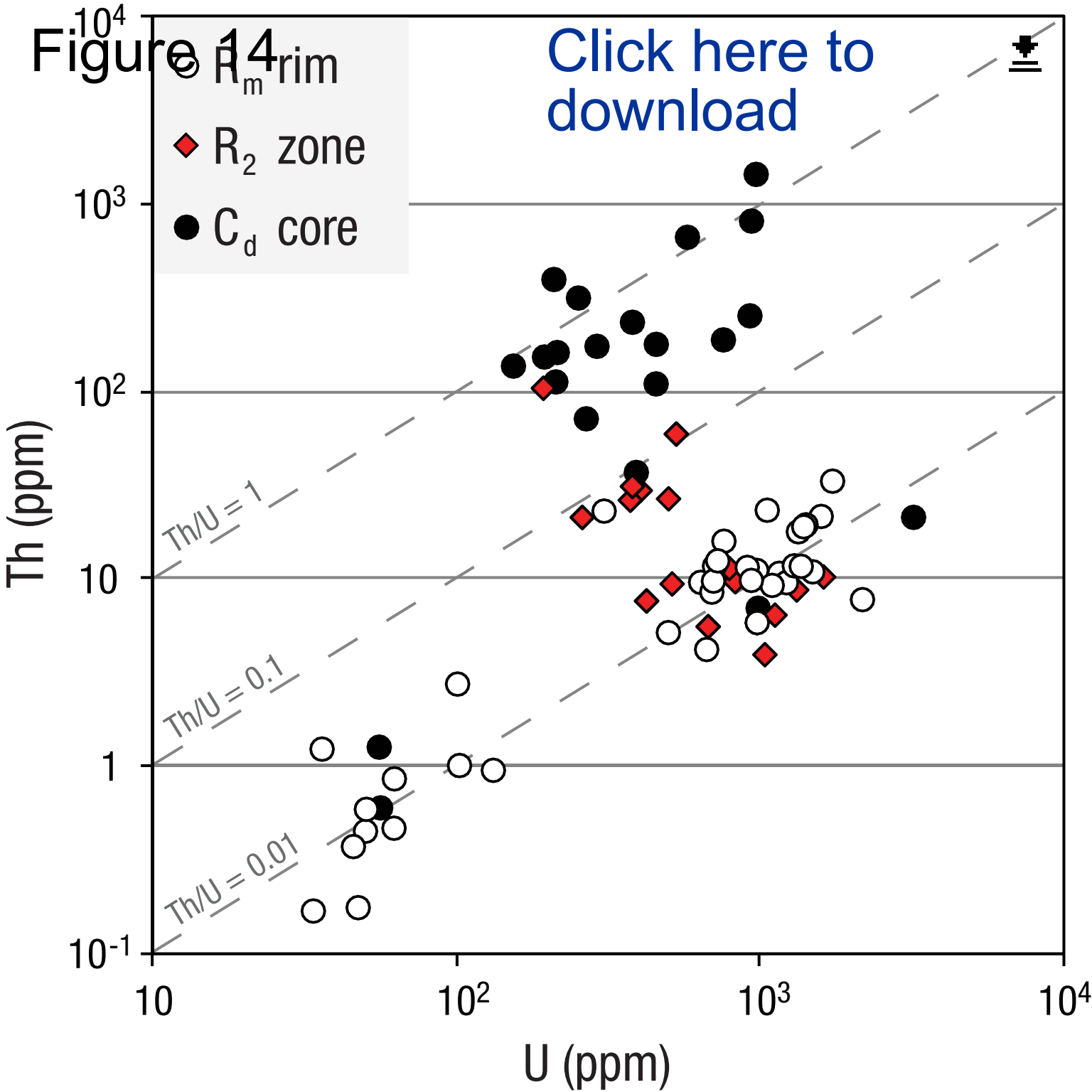
Click here to download
R_m rim
R_2 zone
C_d core
Th/U = 1
Th/U = 0.1
Th/U = 0.01
Th (ppm)
U (ppm)
10^4
10^3
10^2
10
1
10^{-1}
10
10^2
10^3
10^4

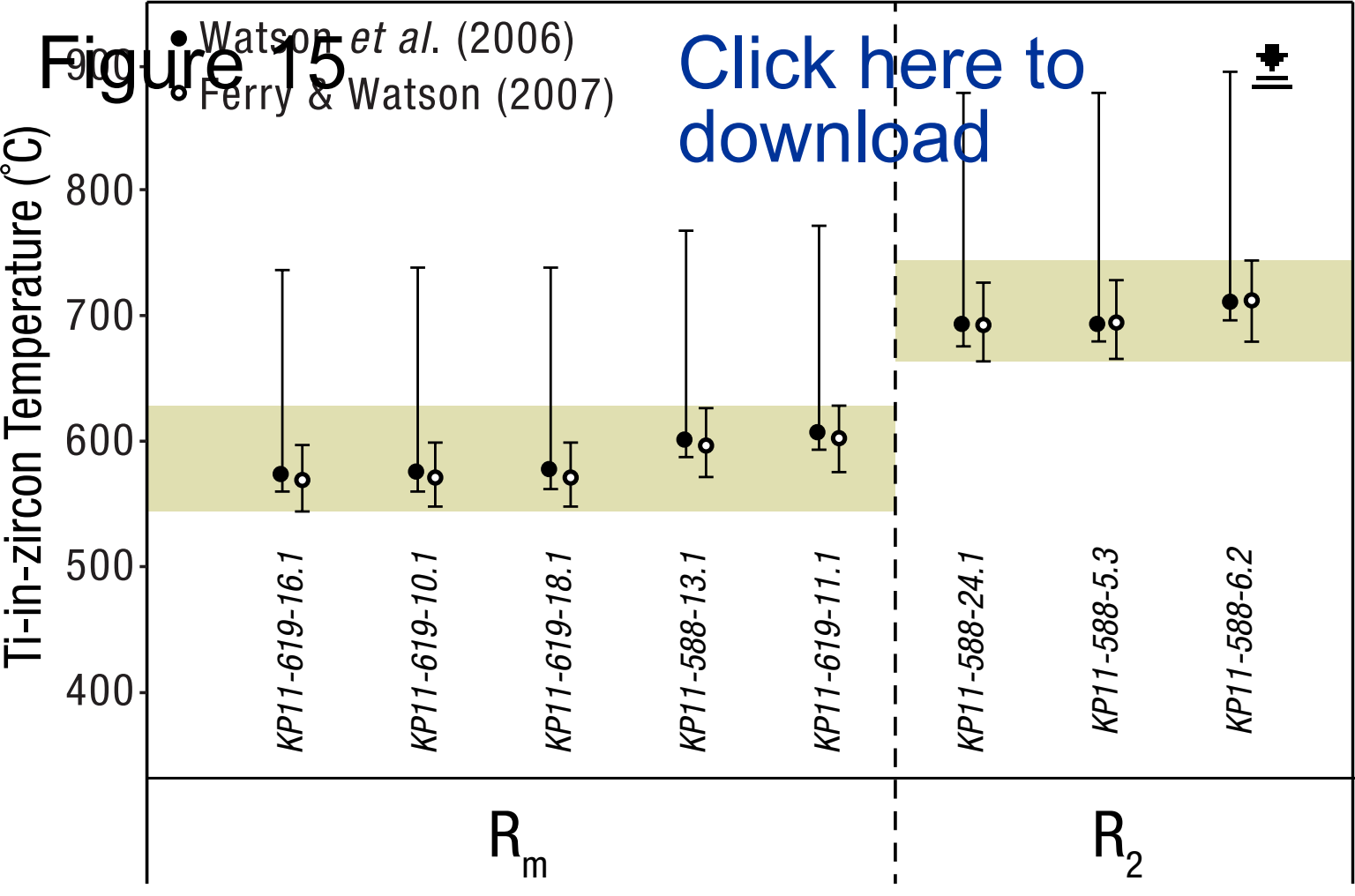
Figure 15
Watson et al. (2006)
Ferry & Watson (2007)
Click here to download
Ti-in-zircon Temperature (°C)
800
700
600
500
400
KP11-619-16.1
KP11-619-10.1
KP11-619-18.1
KP11-588-13.1
KP11-619-11.1
KP11-588-24.1
KP11-588-5.3
KP11-588-6.2
Rm
R2

Figure 16

Click here to download

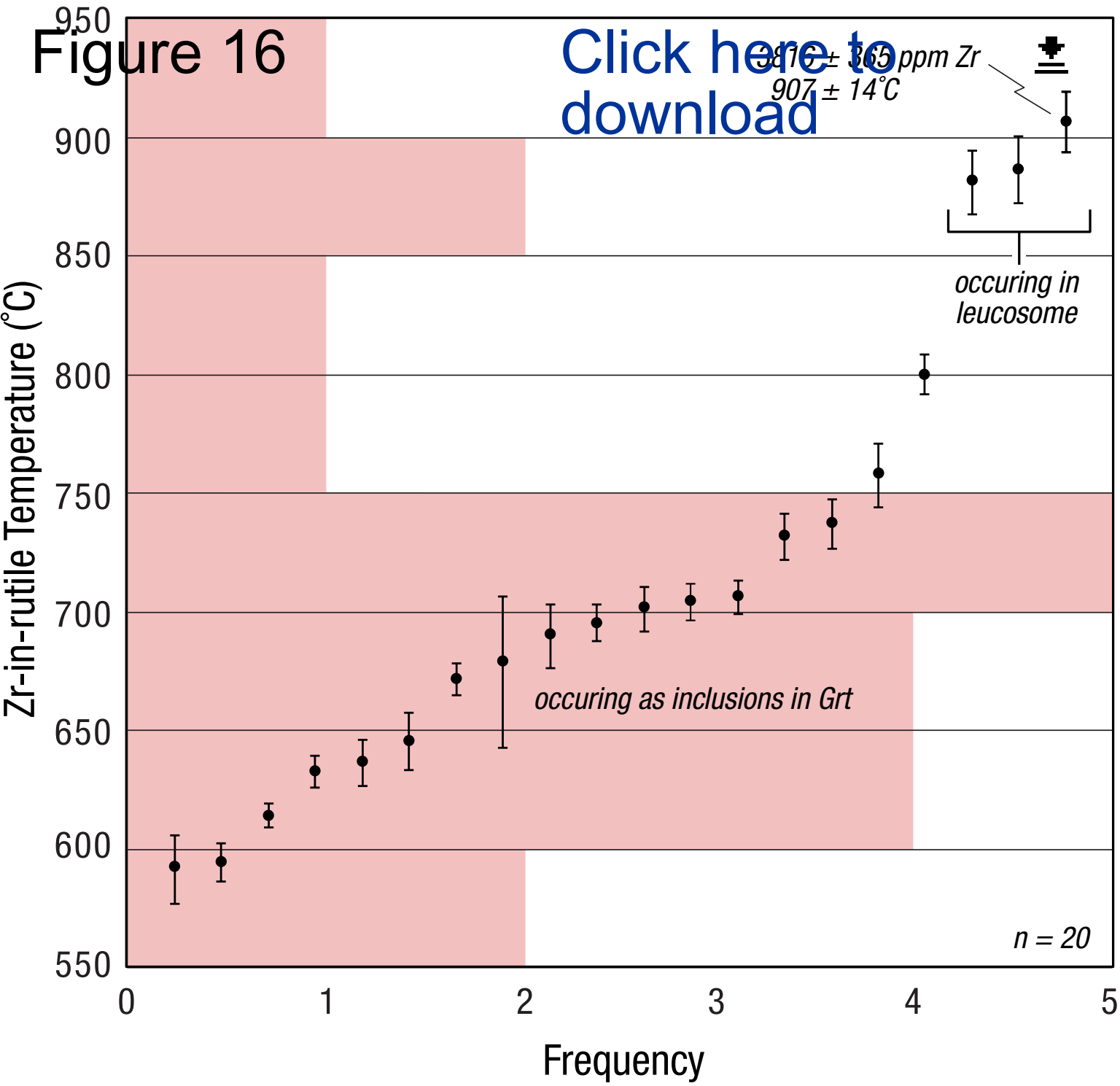

Figure 17

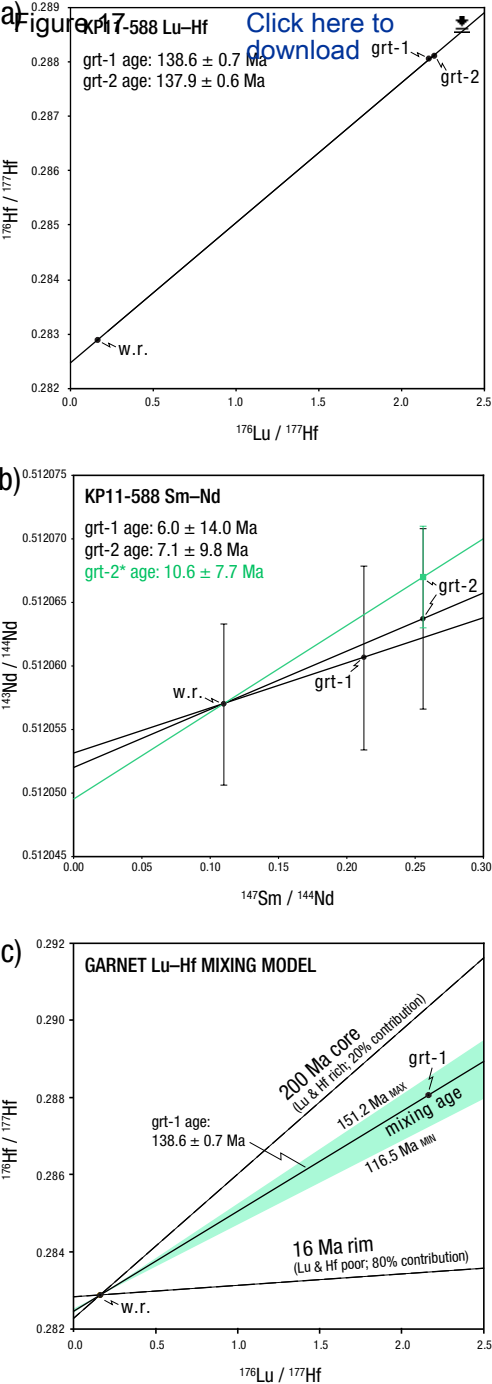
a)
KP11-588 Lu–Hf
grt-1 age: 138.6 ± 0.7 Ma
grt-2 age: 137.9 ± 0.6 Ma
Click here to download
grt-1
grt-2
w.r.
176Hf / 177Hf
176Lu / 177Hf
b)
KP11-588 Sm–Nd
grt-1 age: 6.0 ± 14.0 Ma
grt-2 age: 7.1 ± 9.8 Ma
grt-2* age: 10.6 ± 7.7 Ma
grt-2
grt-1
w.r.
143Nd / 144Nd
147Sm / 144Nd
c)
GARNET Lu–Hf MIXING MODEL
200 Ma core
(Lu & Hf rich; 20% contribution)
grt-1
151.2 Ma MAX
mixing age
116.5 Ma MIN
grt-1 age:
138.6 ± 0.7 Ma
16 Ma rim
(Lu & Hf poor; 80% contribution)
w.r.
176Hf / 177Hf
176Lu / 177Hf

Figure 18

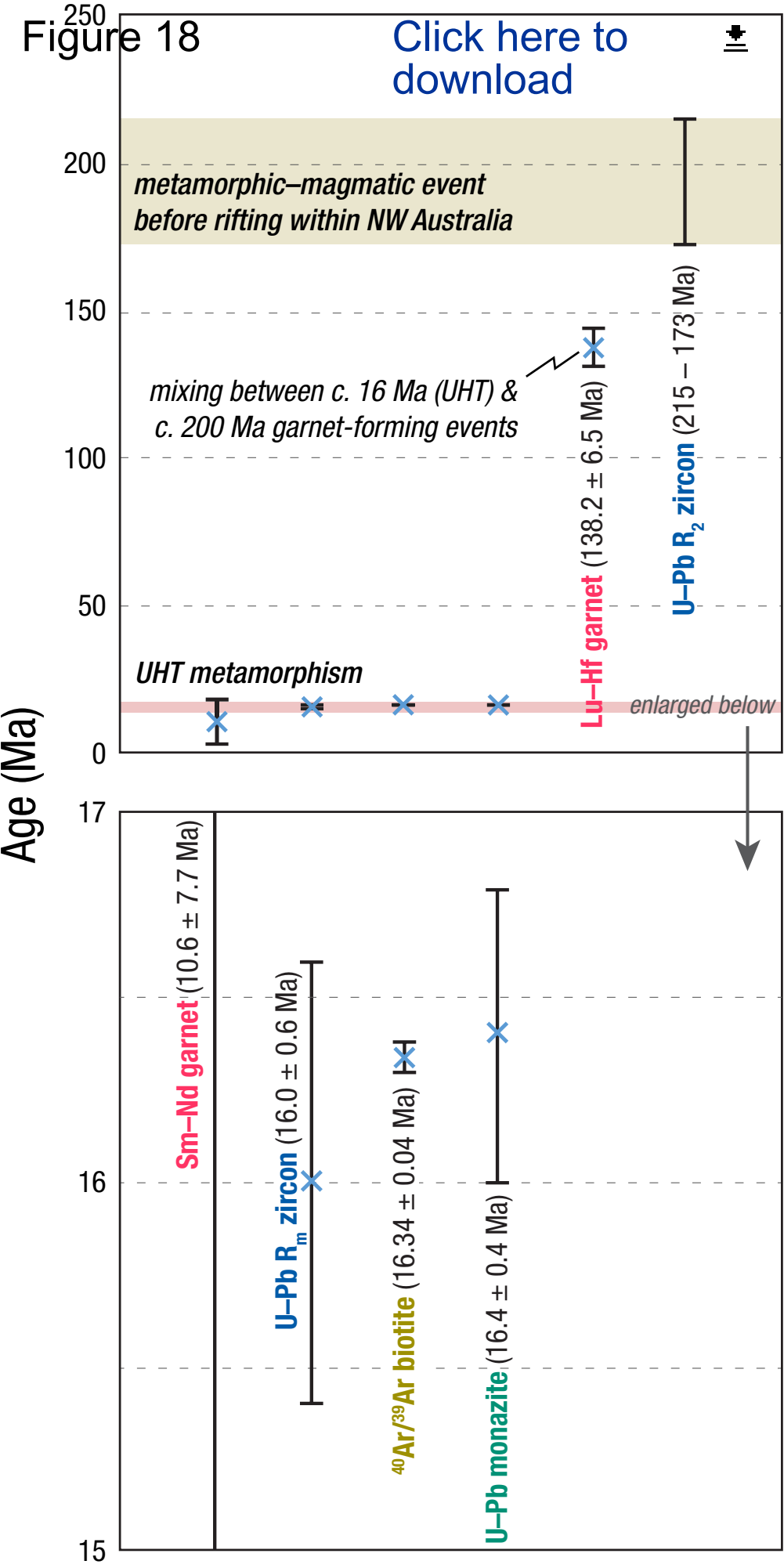

Figure 19

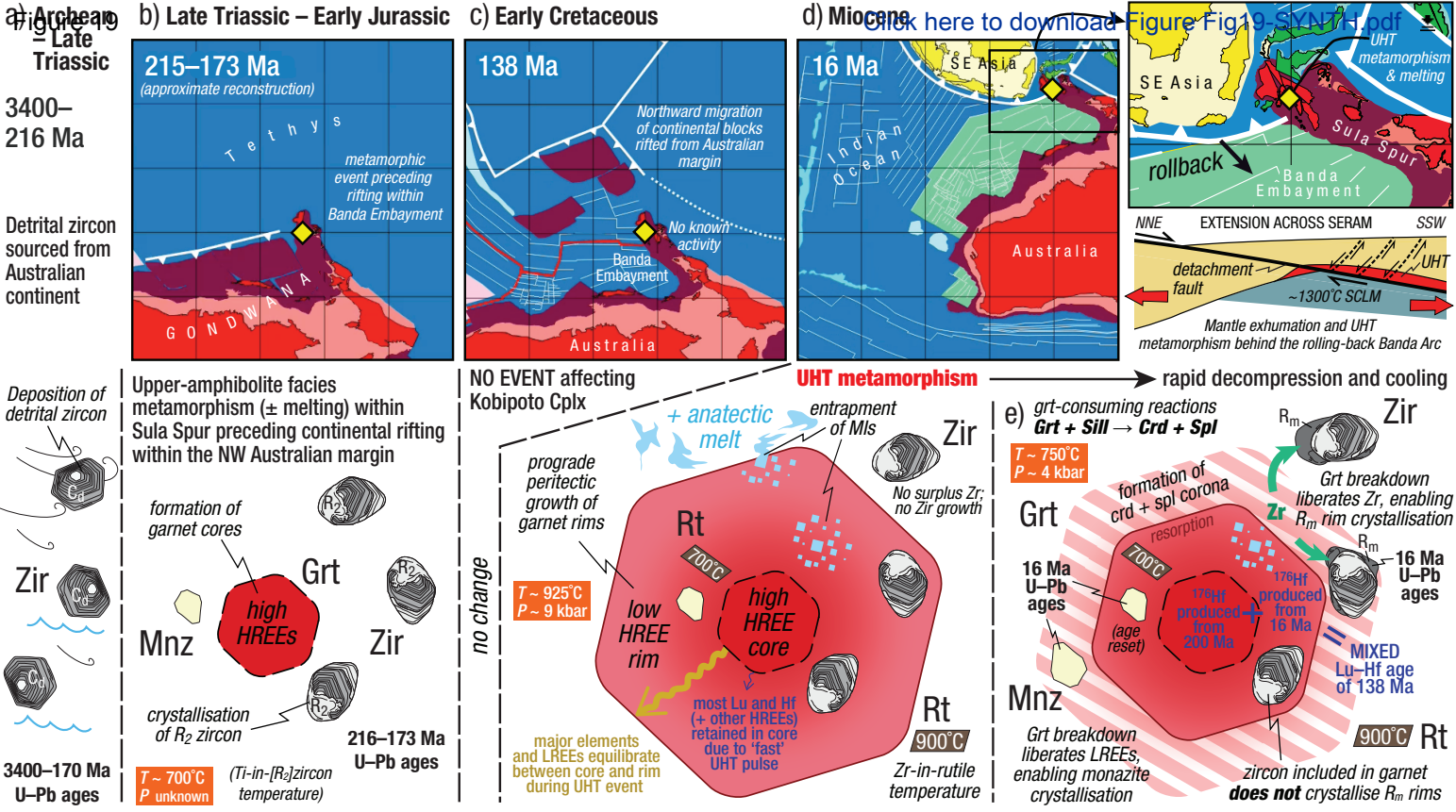

Zircon REE data

Click here to access/download

Dataset

Pownall-etal-ZIR-REE.xlsx

Garnet REE data

Click here to access/download

Dataset

Pownall-etal-GRT-REE.xlsx